Symmetry and Transport in Cold Atom Ratchets

Ralf Gommers

A thesis submitted to University College London
in partial fulfilment of the requirements for the
degree of Doctor of Philosophy

Department of Physics and Astronomy
University College London
June 2007

ProQuest LLC
789 East Eisenhower Parkway
P.O. Box 1346
Ann Arbor, MI 48106-1346

Symmetry and Transport in Cold Atom Ratchets

Ralf Gommers

I, Ralf Gommers, confirm that the work presented in this thesis is my own. Where information has been derived from other sources, I confirm that this has been indicated in the thesis.

....

(signature) (date)

Supervisor: Dr. Ferruccio Renzoni
Reader in Physics

....

(signature) (date)

Abstract

Ratchets are devices that operate away from thermal equilibrium and can rectify zero-mean perturbations to achieve directed transport. We implement a ratchet system by using cold atoms in a driven optical lattice. This ratchet system can be precisely controlled experimentally, by adjusting either the driving parameters or the characteristics of the optical lattice.

Directed transport in our ratchet is caused by rectification of either the driving force or fluctuations. We demonstrate under which conditions these types of rectification occur. Rectification of the driving force is a deterministic process, while rectification of fluctuations implies that the atoms act as Brownian motors. We show that resonant activation is the underlying mechanism of operation of these Brownian motors.

The ratchet transport is controlled by symmetries of the system. The temporal symmetry of the system is normally broken by a time-asymmetric driving force. Here we show that for a system with symmetric driving and a symmetric potential, directed transport can also be caused by dissipation-induced breaking of time-reversal symmetry. This happens in the limit of small driving amplitude and large dissipation.

We also study quasiperiodic driving of a cold atom ratchet and examine the relationship between symmetries and transport in this case. When mapping the route to quasiperiodicity we find a characteristic peak spectrum with transport occurring for certain ratios of frequencies. We characterize these peaks spectroscopically, and conclude that their shape is determined by the duration of driving. Finally, we investigate the coherency of transport with quasiperiodic driving and find large coherencies for certain driving parameters.

To Olga, Mark and Ryu

Acknowledgments

It feels like yesterday that I was at the beginning of my PhD, wondering what the next three years were going to be like. There have been many highlights, and of course a few lows as well, on the way. Overall it has gone quicker and better than I could have hoped for.

First of all I have to thank Ferruccio Renzoni, I really couldn't have wished for a better supervisor. His optimism matched very well with my more realistic outlook, stimulating me to always believe that today was the day everything would come together. And he was right, once every few months. His door was always open, and our daily contacts were very motivating for me.

I shared an office with Peter Douglas for three years, and I thank him for teaching me a lot of what I know about life in Britain. I'll miss his humor and profound knowledge of street culture. I would never have been able to get up to speed with the experiment in such a short time without the help of Phil Jones, who always had time for a quick brainstorm even though he had left the group just before I arrived. Martin Brown impresses everyone by the sheer amount of numerical data he manages to produce, and that has been very valuable when testing new ideas for experiments or confirming old ones. More recently Slav Lebedev, Arne Wickenbrock and Lyubo Petrov have also been welcome additions to the group. With their arrival our group has grown from its humble beginnings to a very collegial and interesting place to be.

I feel I'm lucky to have been able to work at the intersection of two fields - laser cooling and ratchets - that are both developing quickly. I have met many people in both fields that I have worked with very pleasantly, and I found everyone is very willing to share thoughts on problems that occupied me at some points. This ranged from the very technical, for example Aidan Arnold who helped me figure out some problems with

my camera, to the history of the field in which I was working. In that respect the late night bar discussions at Schloss Reisensburg with Sergey Denysov and Sergej Flach were particularly illuminating.

It was fortunate that there is a large laser cooling group just half an hour away at Imperial, and I want to thank especially Jonathan Ashmore and Henry Ashworth for making me feel welcome there. I enjoyed chatting about whatever was going on in our respective labs and running our joint journal club. Bert Claessens deserves a special mention as well, he really showed me the ropes around a cold atom lab when I was a starting Masters student and it was always a pleasure to exchange thoughts on practical problems even after I left for London.

My parents have always supported me in everything I wanted to do, and I'm immensely grateful for that. It probably wasn't easy for them to see me leave the Netherlands for at least three years, but they've managed to hide that from me quite well. My visits to them, infrequent as they were, always re-energized me. One of my personal highlights was being best man at my sister's wedding. I'm sure Olga and Mark will continue to build a great life together and overcome the health problems of their newborn baby Ryu.

Finally, more than anything these three years were defined by my girlfriend Jing. She is absolutely wonderful and I can't imagine not being with her. If I have to work in the weekend she is understanding, if I have some bad luck she'll cheer me up and time flies when we're together. Her spontaneity and outgoing character mean everything to me.

Contents

List of Figures

Chapter 1

Introduction

The field of laser cooling has developed tremendously since the realization of the first magneto-optical trap in 1987 [1] and especially since the creation of the first Bose-Einstein condensate in 1995 [2]. It has since developed from a research subject in and of itself into a tool with which to tackle problems in other fields of physics. One of these fields is statistical physics, and here we discuss the implementation with laser cooled atoms of a topic of statistical physics that is receiving a lot of interest at the moment, ratchets.

1.1 Ratchets

Can one extract useful work from thermal fluctuations? This question has inspired many people to come up with designs for perpetual motion machines. None however have been able to escape the consequences of the Second Law of Thermodynamics. Smoluchowski and Feynman made such a design as well, only with the intention of showing it could never work at thermal equilibrium. This Feynman *ratchet*, discussed in section 1.1.1, is able to rectify fluctuations when operating out if equilibrium. We here define a ratchet as a device exhibiting *directed transport* away from equilibrium as a result of zero-mean fluctuations.

A *Brownian motor* is very similar to a ratchet in that it rectifies fluctuations, the difference is that it operates as a result of *thermal* zero-mean fluctuations. A ratchet on the other hand can operate even in a completely Hamiltonian system with only an external zero-mean driving.

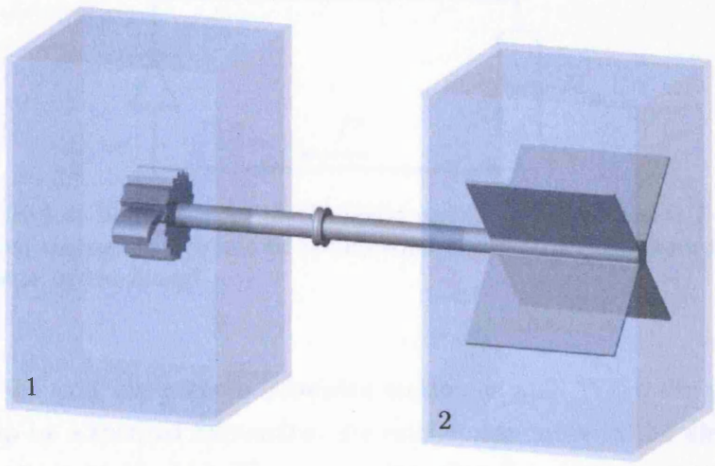

Figure 1.1: Illustration of the Feynman ratchet. The ratchet-and-pawl device in reservoir 1 with temperature T_1 rotates due to thermal fluctuations in reservoir 2 with temperature T_2. The pawl is designed to rectify the unbiased fluctuations in reservoir 2, resulting in unidirectional rotation and the possibility of doing work on a mass connected to the axle.

Note that both ratchets and Brownian motors do consume energy to stay away from equilibrium, hence the Second Law is not violated.

1.1.1 The Feynman ratchet

Perhaps the most well-known ratchet system is the Feynman ratchet. He extended an earlier *gedanken* experiment of Smoluchowski [3] on the possibility of extracting energy from microscopic fluctuations. The basic idea was to use a device with a single axle with on one side a ratchet-and-pawl, a cog with asymmetric teeth and a lever, and on the other side large fins. Due to Brownian motion the surrounding gas randomly pushes on the fins, and the pawl ensures that the axle can rotate only in a single direction. At first sight it is plausible that this device, as shown in figure 1.1, can lift up a mass connected to the axle and thereby do useful work.

Feynman showed however that if the whole system is at thermal equilibrium no useful work can be extracted from the Brownian motion of the gas. This is because the pawl, microscopic in size itself to allow any rota-

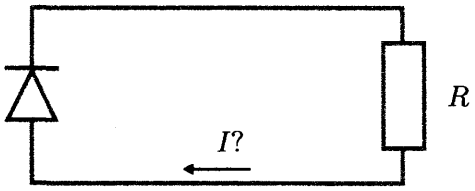

Figure 1.2: Illustration of the Brillouin rectifier. Can a current I be driven through the circuit by rectification of Johnson noise from the resistor by the diode?

tion of the axle, experiences Brownian motion as well. When the pawl is lifted up by a thermal fluctuation the ratchet can move in the direction that is otherwise blocked. The net result is that the rotation rates to the left and the right are exactly equal. If this were not the case, the pawl would be a classical example of a Maxwell's demon.[1] Extraction of work is possible if the temperature of the gas surrounding the fins is larger than that surrounding the ratchet. Though in that case the Second Law does not apply, and the system is simply a microscopic heat engine.

1.1.2 Brillouin's paradox

Another early thought experiment trying to rectify thermal fluctuations was an electrical circuit by Brillouin [5]. It simply consists of an electrical diode and a resistance, as shown in figure 1.2. If the whole circuit is in thermal equilibrium at temperature T the resistance will produce Johnson noise, with a power spectral density per Hz of $\overline{V}^2 = 4k_BTR$. This means there is a fluctuating voltage over the diode which it can rectify, and enough of these circuits in series could form a battery.

The resolution of this paradox lies in the microscopic dynamics responsible for the behavior of the diode. The familiar voltage-current characteristic of the diode is obtained only after averaging over thermal fluctuations and is therefore not valid for our purpose. It can be shown [6] that the $V - I$ curve for thermal fluctuations is shifted with respect to

[1]The demon, brought into life by Maxwell to demonstrate the statistical nature of the Second Law, is still of interest. The last major insight it gave rise to connects statistical physics to information theory. Landauer and Bennett found that information is linked to entropy and that memory erasure of the demon increases the entropy of the system [4].

the one normally used, restoring detailed balance and obeying the Second Law.

1.1.3 Directed transport

The ratchets of Feynman and Brillouin were designed to show the consequences of the Second Law, and to paradoxically not work at equilibrium. One can however turn this around and start thinking about designing devices that operate away from equilibrium and do useful work without violating the Second Law. An interesting step in this direction was made by Tsong and Astumian [7], who in 1986 proposed the flashing ratchet as the mechanism on which some classes of molecular motors operate. Molecular motors are proteins that live in a noisy environment in the human body, and convert random 'kicks', experienced when converting ATP to ADP, in directed motion with the help of a spatially asymmetric potential. This enables them to move a load around the body. Providing insight into the mechanism of operation of molecular motors was one of the motivations for the recent surge in interest in ratchets.

Ajdari and Prost [8] in 1992 and Magnasco [9] in 1993 emphasized the broader significance of ratchets, when they showed that *directed transport* is a generic feature of a system out of equilibrium and with broken symmetry. This quickly led to a host of theoretical work [10–15] as well as experimental demonstrations of ratchets with colloidal particles [16] and optically trapped beads [17]. It did not take long before new technological applications appeared on the horizon.

1.1.4 Applications

A promising development is the use of ratchets as particle separation devices. It has been shown that particles with different properties like size or mass can be made to move in opposite directions [16]. This has already enabled separation of phospholipid molecules [18], and can be applied to many other types of molecules even in their native environment, something that is very hard to do any other way.

Other applications for ratchets include electron pumps [19], vortex density control in superconductors [20] and nanoscale machinery [21]. Finally, ratchets are also interesting from the point of view of theoretical

non-equilibrium thermodynamics. This includes classical [9] and quantum [22] transport phenomena as well as a test for recently discovered fluctuation theorems [23].

In chapter 4 we will discuss the properties of ratchets in detail and give an overview of the different techniques used to create ratchets.

1.2 Laser cooling and trapping

Laser cooling was first proposed in 1975 by Hänsch and Schawlow [24] as a method to cool down atomic gases. With the required laser technology available, atoms were first cooled in a so-called optical molasses in 1985 by Chu *et al.* [25]. This was quickly followed by the demonstration of the first magneto-optical trap (MOT) in 1987 by Raab *et al.* [1], and provided a very convenient and robust way to trap large numbers of atoms. MOTs have been the workhorse of atomic physics ever since. They are easy to set up, robust tools that can rapidly capture a large number of atoms from a background gas or collimated beam and cool and trap them. A MOT typically contains $10^8 - 10^{10}$ atoms at a temperature of about 100 μK. The most commonly used species are alkali atoms such as Rb, Cs and Na, but a wide range of other atoms (noble gases, group II atoms) can also be trapped.

The interest in laser cooling increased massively when in 1995 Cornell, Wieman and collaborators created for the first time a long sought-after state of matter, a Bose-Einstein condensate (BEC) [2]. This is a quantum state of matter where every atom has exactly the same wave function, and has allowed for precise control over and manipulation of a mesoscopic quantum object. More recently, DeMarco and Jin were able to create quantum degenerate gases of fermions as well [26].

In the rest of this section we will discuss the basic physics of laser cooling and trapping.

1.2.1 Laser cooling

The most frequently used and most robust of many laser cooling schemes is laser Doppler cooling. The idea behind Doppler cooling is simple: let an atom scatter photons from a laser beam that is propagating in a direc-

tion opposite to the atom, thereby slowing down the atom. In practice this can be accomplished by an optical molasses, i.e. by irradiating the atom from all sides with light that is slightly red detuned from atomic resonance. The Doppler shift of the light, $\delta_D = -\boldsymbol{k} \cdot \boldsymbol{v}$, will then ensure that the counter-propagating light is shifted closer to resonance and the co-propagating light further away from it.

The momentum transfer when a photon gets absorbed is $\hbar\boldsymbol{k}$, which slows down the atom. The atom gets another momentum kick when the atom returns to the ground state by spontaneously emitting a photon after a time $\tau \approx \Gamma^{-1}$, with Γ the natural linewidth of the atomic transition, but this time in a random direction. After n such absorption-emission cycles the kicks from the spontaneous emission average to zero, and the momentum of the atom has decreased by $n\hbar k$. For a two-level atom the force due to a single laser beam can be expressed as [27]

$$\boldsymbol{F} = \hbar\boldsymbol{k}\frac{s_0\Gamma/2}{1 + s_0 + [2(\delta + \delta_D)/\Gamma]^2}. \tag{1.1}$$

Here $s_0 = I/I_s$ is the saturation parameter, with I the intensity of the laser beam and $I_s = \frac{\pi hc\Gamma}{3\lambda^3}$ the saturation intensity,[2] and $\delta = \omega - \omega_a$ the detuning of the laser frequency ω from atomic resonance ω_a. For laser beams coming from both sides the force depends on the atom velocity $\boldsymbol{v}$ in such a way that the force is approximately linear with the velocity:

$$\boldsymbol{F_{OM}} \simeq -\frac{8\hbar k^2 \delta s_0}{\Gamma(1 + s_0 + (2\delta/\Gamma)^2)^2}\boldsymbol{v} = -\alpha\boldsymbol{v}. \tag{1.2}$$

This force is a friction force, it can slow down atoms to micro-Kelvin temperatures, but since there is no position-dependence in (1.2) it cannot trap them. For that we need a magneto-optical trap.

1.2.2 Magneto-optical trapping

A MOT is formed by three orthogonal pairs of counter-propagating laser beams with at the point where they cross a magnetic quadrupole field, formed by two coils in anti-Helmholtz configuration. Each of these pairs

[2]For an on-resonance laser beam with $I = I_s$, the atomic excited-state population is 1/4, for $I \gg I_s$ it approaches 1/2.

has one beam that is σ^+ and one that is σ^- polarized. We now explain the principle of the MOT for an atom on a $J_g = 0 \rightarrow J_e = 1$ transition.

The magnetic field induces a Zeeman shift in the magnetic sub-levels of the atom, so the degeneracy of these levels is broken. This is illustrated in figure 1.3. On the left side of the center of the trap the $m_J = +1$ sub-state is shifted closer to resonance, and the $m_J = -1$ further away from resonance. This means the atom will be pumped to the $m_J = +1$ state and interact mainly with the σ^+-polarized beam, which pushes the atom towards the center of the trap. The opposite happens on the right side of the trap center so that, in addition to the velocity-dependent force (1.2), we now have a spatially dependent force. The total force on an atom in a MOT is now given by

$$\boldsymbol{F_{MOT}} = -\alpha \boldsymbol{v} - \frac{\alpha g \mu_B}{\hbar k} \left| \frac{d\boldsymbol{B}}{d\boldsymbol{r}} \right| \boldsymbol{r}, \tag{1.3}$$

where g is the Landé factor, μ_B the Bohr magneton and $\frac{dB}{dr}$ the gradient of the magnetic field.[3] From (1.3) it can be seen that the motion of an atom trapped in a MOT is that of a damped harmonic oscillator.

1.2.3 Optical lattices

An optical lattice is a periodic structure consisting entirely of light, capable of trapping atoms and in some cases also cooling them. It arises when multiple laser beams are superposed, giving rise to a periodic modulation of light intensity and/or polarization. The name 'optical lattice' was introduced to highlight the analogy with solid-state crystals, which have their atoms arranged in lattices. The analogy is not perfect however as in an optical lattice most lattice sites usually remain empty.[4] In contrast to solid state materials, optical lattices are defect-free and its parameters such as potential depth and lattice spacing are easily tunable. Therefore an optical lattice allows one to implement many states and phase transitions familiar from solid state physics, such as the Mott

[3]This force is not isotropic, because the magnetic gradient along the direction connecting the centers of the coils is twice that of the gradient in the directions perpendicular to it.

[4]Nowadays it is possible to fill every lattice site with the same number of atoms by loading a Bose-Einstein condensate in a lattice and creating a Mott insulator state.

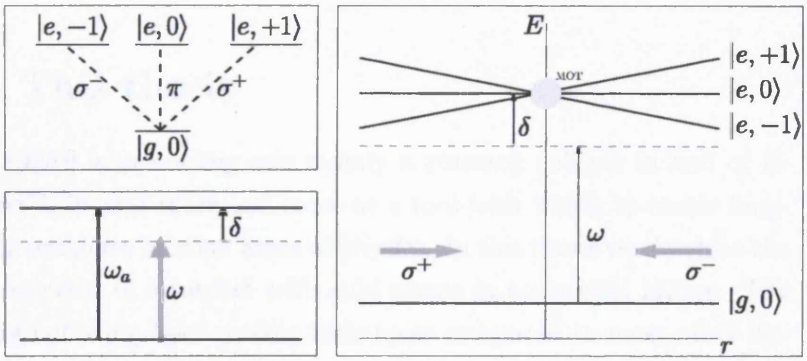

Figure 1.3: Illustration of the principle of a magneto-optical trap (MOT), for an atom on a transition $J_g = 0 \rightarrow J_e = 1$ (top left). The laser frequency ω is detuned from the atomic transition ω_a by $\delta = \omega - \omega_a$ (bottom left). The energy levels of the magnetic substates are position-dependent, due to the MOT magnetic field $\boldsymbol{B} = B_r \boldsymbol{e}_r$, causing the atom to scatter light from the counter-propagating laser beam (right).

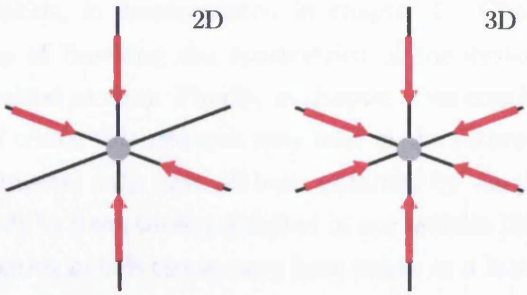

Figure 1.4: Laser configurations for a 2D and a 3D lattice. Many other laser configurations are possible.

insulator state [28] and the BEC-BCS transition [29, 30]. Due to the precise control over the lattice parameters it has also been possible to implement some paradigmatic models of statistical physics, such as the kicked rotor [31] and, more recently, the Feynman ratchet [32].

An illustration of possible laser configurations for 2D and 3D optical lattices is shown in figure 1.4. In chapter 3 we will discuss optical lattices in more detail and show measurements on the temperature and damping

rate of atoms in our optical lattice.

1.3 This thesis

In the 1990's laser cooling was mainly a research subject in and of itself. Now it is used more and more as a tool with which to tackle long-standing problems in other areas of physics. In this thesis we describe the implementation of a ratchet with cold atoms in an optical lattice. The advantage of using laser cooling techniques compared to most other implementations is that the system is very clean, i.e. the optical potential is free of defects and the system (atoms + light) is almost completely decoupled from the environment. Therefore it is an ideal testbed for theory.

In chapter 2 we describe our experimental setup, in chapters 3 and 4 we discuss optical lattices and ratchets respectively in more detail. Then in chapters 5, 6 and 7 we present measurements on our ratchet. The underlying mechanism of the directed motion in the optical potential, resonant activation, is demonstrated in chapter 5. Chapters 6 and 7 show two ways of breaking the symmetries of the system in order to obtain this directed motion. Finally, in chapter 8 we conclude and try to give an idea of where this research may lead in the future.

The experimental data have all been obtained by the present author. Where figures differ from those published in our articles [33–36], the data used for the figures in this thesis have been taken at a later date and are more comprehensive. The data for the numerical simulations presented in figure 4.6 were kindly supplied by S. Denisov.

Chapter 2

Experimental setup

To perform an experiment with optical lattices a few basic steps are needed. First cold atoms, in our case caesium atoms, are collected in a magneto-optical trap. Then they are cooled further in an optical molasses. The optical lattice can then be turned on and, after waiting for a few milliseconds to let the atoms equilibrate, an experiment can be performed. Finally a detection method, usually some form of imaging, is used to measure what has happened. In this chapter we discuss the details of the experimental setup and how it is used to perform this basic *capture-cool-experiment-detect* cycle, as shown in figure 2.1.

2.1 Laser system

To operate a ^{133}Cs MOT, laser light on the cooling transition ($F = 4 \rightarrow F' = 5$) and on the repumping transition ($F = 3 \rightarrow F' = 4$) is needed. Therefore two external cavity diode lasers are used that are locked close to these transitions by saturated absorption spectroscopy [37]. The design of our home-built diode lasers is shown in figure 2.2. The grating directs the light from its first order back into the laser diode, forming a cavity. The grating mount is controlled by a piezo-electric element, which can be used to change the angle of the grating and thus tune the cavity length. This is one way to control the frequency of the laser light, the other ones are by changing the temperature of and the current through the diode. For normal operation the temperature is kept constant, slow drifts of the frequency are compensated for by changing the grating angle and fast

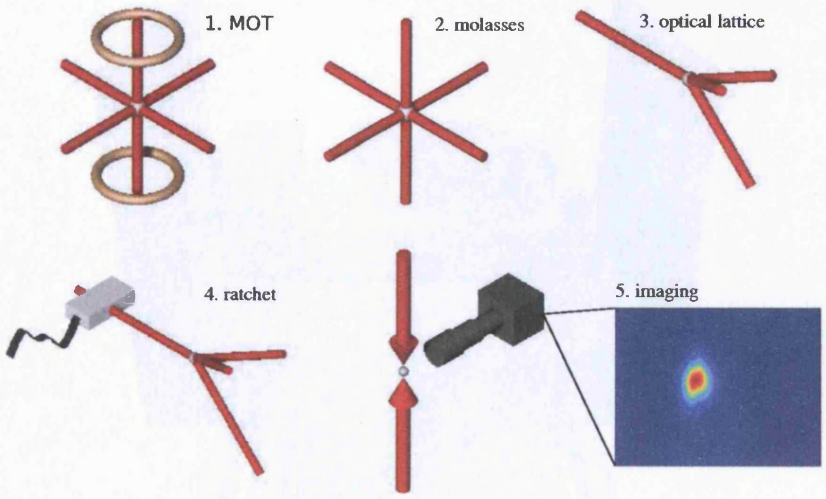

Figure 2.1: Illustration of the phases of the experiment. First, the MOT is loaded for a few seconds. The atom cloud is then cooled further by optical molasses and loaded into the optical lattice. After applying a frequency modulation to one of the lattice beams to create a ratchet (see section 5.2 for details), the final result is obtained by fluorescence imaging.

($>$ 1 kHz) noise is compensated for with the diode current.

The laser locked close to the cooling transition is used to injection lock [39] two free-running 'slave' diode lasers. This gives us two high power ($\approx$ 100 mW) laser beams tuned to the right transition with minimal complexity. One of these slave lasers, the slave referring to the following of the frequency of the grating-stabilized 'master' laser, is used for the MOT and the other one for the optical lattice.

The master laser is locked to the $F = 4 \rightarrow F' = 4/5$ crossover transition [40], which is 125.5 MHz red detuned from the cooling transition. The frequency of the MOT beams is shifted to the right frequency ($\delta = -2\Gamma$) by two acousto-optical modulators (AOMs), one fixed at -80 MHz and the other one an adjustable double pass AOM with a range from 78 to 102 MHz. The repumper laser is locked to the $F = 3 \rightarrow F' = 3/4$ cross-over transition and shifted onto resonance ($F = 3 \rightarrow F' = 4$) by a single fixed-frequency AOM. The measured absorption spectra and error signals with the lock points are shown in appendix A.

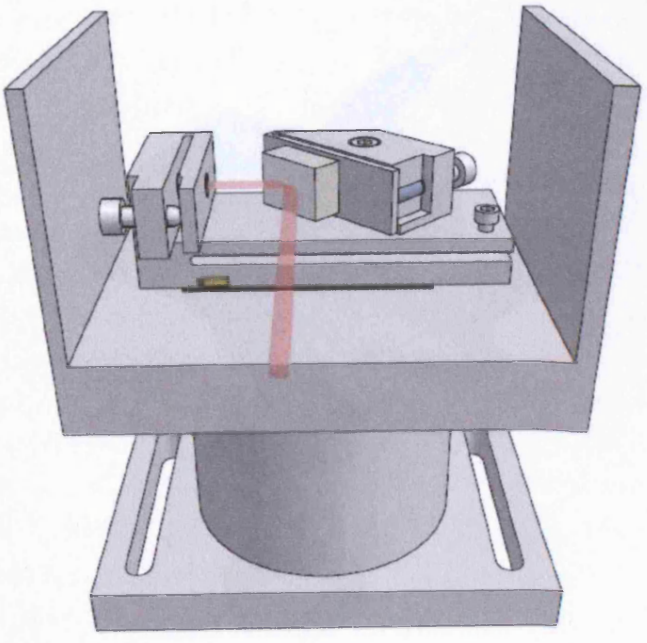

Figure 2.2: Artist's impression of a grating-stabilized diode laser in the Littrow configuration, design as in Ricci *et al.* [38]. Shown are the laser diode mount, grating and grating mount, base plate, thermoelectric cooling element, thermistor and housing. The slave lasers do not possess a grating but are otherwise the same. Anamorphic prisms to make the laser beam circular are positioned outside the laser and are not shown here.

2.2 Vacuum system

The pressure required to do experiments with optical lattices is below 10^{-8} mbar. This ensures that the atoms are not lost from the lattice because of collisions with background atoms on the timescale of a typical experiment ($\sim$ 50 ms). The design of the vacuum system is such that this pressure is reached even without baking it. Its total volume is about two liters, a large part of which is the glass cell in which the experiments take place. The cell is connected by a valve to a glass capsule containing solid caesium. This valve has to be opened only every few months when the caesium is starting to run low in the cell. Simply heating the caesium with a heatgun is enough to refill the glass cell. Two pumps, an ion pump (Varian StarCell, 20 l/s) and a non-evaporable getter pump (SAES

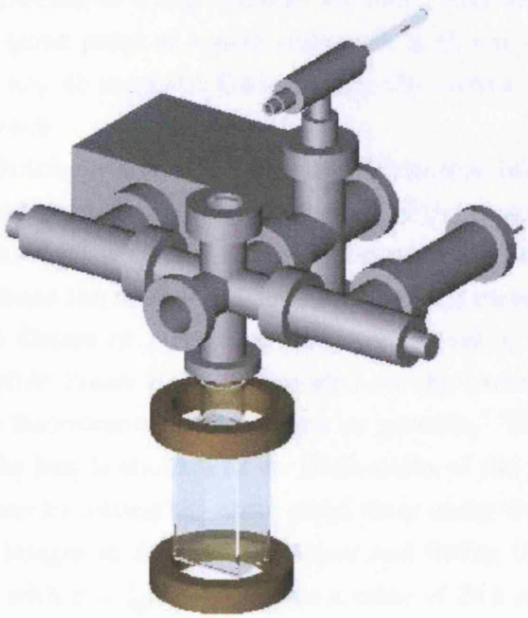

Figure 2.3: Artist's impression of the vacuum system. Shown are the glass cell, caesium capsule, pumps, stainless steel tubes and valves, as well as the MOT coils.

ST101, 20 l/s), maintain a pressure of about $5 \cdot 10^{-9}$ mbar. The pumps both have a valve as well to control the pumping speed. The vacuum system is shown in figure 2.3.

2.3 MOT and optical lattice

The MOT is formed by three pairs of retroreflected beams that cross at the center of the glass cell. The two coils that generate the quadrupole field for the MOT have 170 turns each, a diameter of 12 cm and they are separated by 12 cm as well. A current of 2.75 A through the coils gives the required gradient of about 10 G/cm at their center. The MOT beams are 1 cm in diameter, have an intensity of 2.5 mW/cm^2 and are detuned by -2Γ. This gives a MOT which contains on the order of 10^8 atoms at a typical temperature of about 100 μk. The MOT is monitored continuously by a simple charge-coupled device (CCD) camera (Watec

WAT902H) connected to a monochrome monitor. The whole system is surrounded by three pairs of square coils with a 45 cm diameter that compensate for any dc magnetic field - mainly the earth's magnetic field - present in the cell.

A thermo-electrically cooled CCD camera (Princeton Instruments MicroMax) is used to obtain fluorescence images of the atom cloud at the end of an experimental cycle. An on-resonance, retro-reflected laser beam is used to illuminate the atoms for 1 ms. This beam is carefully balanced in order not to distort or push away the atom cloud in this time. A zoom lens (Navitar Zoom 7000) is mounted on the camera to capture as much of the fluorescence of the atoms as possible. The solid angle subtended by the lens is about 0.12 sr. Calibration of the magnification of the lens is done by letting the atom cloud drop under the influence of gravity, taking images at different fall times and fitting the position of the atom cloud with $x = \frac{1}{2}gt^2$. This gives a value of 28.5 μm/pixel, or a magnification of 4.25.

The arrangement of the optics to prepare all the beams for the MOT and the optical lattice is shown schematically in figure 2.4. The glass cell is large enough to accommodate all beams, with the MOT beams coming in at a 90° angle with the sides of the cell. The lattice is formed by four beams in the umbrella configuration, as discussed in section 3.1.4. The two AOMs used for the lattice beams are driven by phase-locked function generators (Rohde & Schwarz SMY01) that can be frequency modulated to create a ratchet force, as described in section 5.2. This frequency modulation comes from two or three other phase-locked function generators (Agilent 33220A). The axial lattice beam comes in under a very slight angle with one of the MOT beam pairs, the other three beams come in under an angle of 30°. The probe beam finally comes in at an angle of 7° with the axial lattice beam.

The optical lattice can be characterized by the oscillation frequency of the atoms in the potential wells and the scattering rate of photons, as discussed in chapter 3. In practice these parameters are tuned by varying the intensity and detuning of the lattice beams. The intensity is controlled by the last two AOMs the beams go through (bottom left in figure 2.4). The detuning is set by two double-pass AOMs, one in the lock path of the master laser (not shown) and one right before the master

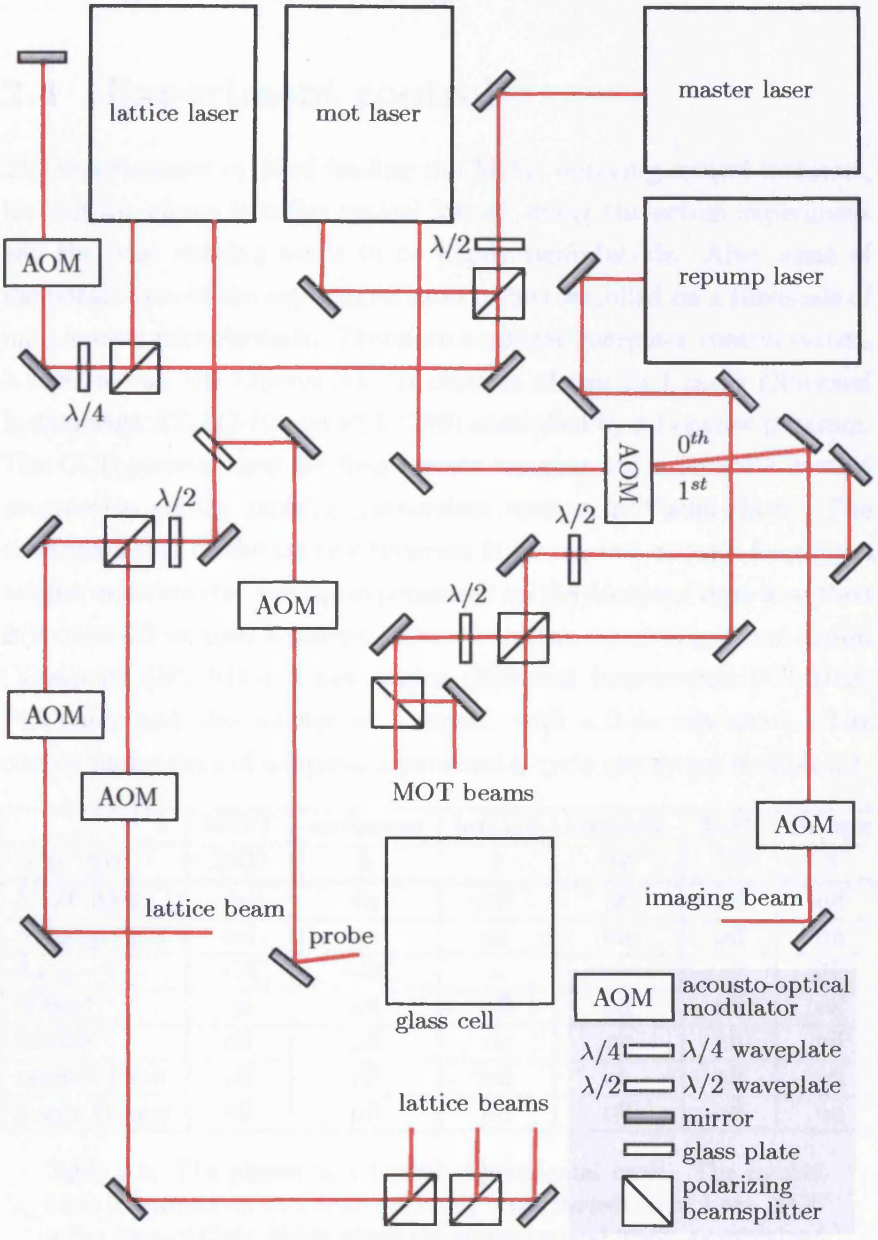

Figure 2.4: Schematic layout of the optical table. The optics for locking the laser frequency to the transition and for injecting the slave lasers are not shown.

beam injects the lattice (top left in figure 2.4). This gives a range from -5Γ to -25Γ for the lattice detuning.

2.4 Experiment control

The experimental cycle of loading the MOT, applying optical molasses, loading the atoms into the optical lattice, doing the actual experiment and the final imaging needs to be highly reproducible. Also, some of the parameters of the experiment need to be controlled on a timescale of milli or even microseconds. Therefore a reliable computer control system is used to run the experiment. It consists of two PCI cards (National Instruments AT-AO-10 and PCI-1200) controlled by a Labview program. The CCD camera used for fluorescence imaging has a separate control program to set the imaging parameters written in Visual Basic. The time resolution of the control program is 50 μs, fast enough for all the ratchet experiments. For the experiments on the damping time described in section 3.3 we used a different control system, consisting of one digital (Viewpoint DIO-64) and two analog (National Instruments PCI-6713) PCI cards and also written in Labview, with a 2 μs resolution. The control parameters of a typical experimental cycle are shown in table 2.1.

	MOT	**molasses**	**lattice**	**ratchet**	**TOF**	**image**
time (ms)	2000	5	2	30	10	3
MOT light	on	on	off	off	off	off
repump light	on	on	on	on	off	on
δ_{MOT}	-2Γ	-3Γ	-	-	-	0Γ
B field	on	off	off	off	off	off
lattice	off	off	on	on	off	off
ratchet force	off	off	off	on	off	off
image trigger	off	off	off	off	off	on

Table 2.1: The phases of a typical experimental cycle. The ratchet force is ramped up and down smoothly when turned on in 1 ms. TOF is the time-of-flight phase where the atoms expand freely, as explained in section 3.3. The duration of lattice and ratchet phases is varied slightly for different experiments.

Chapter 3

Optical lattices

As we saw in chapter 1, optical lattices are periodic potentials for cold atoms formed by the interference of two or more laser beams. We can classify these lattices as near-resonant or far-off-resonance, depending on the rate at which the atoms in the lattice scatter photons. For near-resonant lattices we usually need to consider only a single optical transition, while the internal state of the atoms trapped in such a lattice can change frequently. For far-off-resonance lattices on the other hand we need to consider multiple optical transitions, while the internal state of the atoms in the lattice does not change. We will concern ourselves only with near-resonant, bright optical lattices. The discussion on the light shift and the calculation of potential depth in sections 3.1.1 and 3.1.5 are equally valid for far-off-resonance lattices however. In the rest of this chapter we will discuss the structure and cooling mechanism of optical lattices, how we can probe this structure and finally we characterize our own lattice.

3.1 Lattice structure

3.1.1 Light shift

The optical potential for an atom in an optical lattice is given by the light shift, or ac Stark shift, of the atomic energy level that is the ground state of the optical transition. We will now derive the magnitude of the light shift for an atom as a function of laser intensity and polarization, following the notation used in [41].

The electric field of a laser beam is given by

$$\boldsymbol{E}_L(\boldsymbol{r},t) = \boldsymbol{E}_L^+(\boldsymbol{r})e^{-i\omega_L t} + \boldsymbol{E}_L^-(\boldsymbol{r})e^{+i\omega_L t}, \tag{3.1}$$

where $\boldsymbol{E}_L^+$ ($\boldsymbol{E}_L^-$) are the positive (negative) frequency components of the electric field of the laser. We can define these electric field components as $\boldsymbol{E}_L^\pm = \pm\frac{1}{2}\boldsymbol{\varepsilon}(\boldsymbol{r})\varepsilon_L(\boldsymbol{r})$, with $\boldsymbol{\varepsilon}(\boldsymbol{r})$ the polarization vector and $\varepsilon_L(\boldsymbol{r})$ the electric field amplitude. The atom-laser interaction Hamiltonian is given by

$$V_{AL} = -\boldsymbol{d}\cdot\boldsymbol{E}_L(\boldsymbol{r},t) = -\boldsymbol{d}^+\cdot\boldsymbol{E}_L^+(\boldsymbol{r})e^{-i\omega t} - \boldsymbol{d}^-\cdot\boldsymbol{E}_L^-(\boldsymbol{r})e^{+i\omega t}, \tag{3.2}$$

where $\boldsymbol{d}^+$ ($\boldsymbol{d}^-$) are the dipole operators for the transition from ground to excited (excited to ground) states.

The light shift operator is given by

$$\Lambda(\boldsymbol{r}) = \left(\boldsymbol{\varepsilon}^*(\boldsymbol{r})\cdot\hat{\boldsymbol{d}}^-\right)\left(\boldsymbol{\varepsilon}(\boldsymbol{r})\cdot\hat{\boldsymbol{d}}^+\right), \tag{3.3}$$

with $\hat{\boldsymbol{d}}^\pm$ reduced dipole operators. When we choose the basis vectors for the polarization vector as

$$\boldsymbol{\varepsilon}_\pm = \mp\frac{1}{\sqrt{2}}(\boldsymbol{\varepsilon}_x \pm i\boldsymbol{\varepsilon}_y) \qquad\qquad \boldsymbol{\varepsilon}_0 = \boldsymbol{\varepsilon}_z, \tag{3.4}$$

corresponding to $\sigma^\pm$ and π polarizations respectively, then the light shift operator $\Lambda(\boldsymbol{r})$ reduces to the product of two matrices of Clebsch-Gordan coefficients. The light shift operator, together with the detuning and intensity of the laser field, will give us the effective Hamiltonian

$$H_{eff}(\boldsymbol{r}) = \hbar\delta s(\boldsymbol{r})\Lambda(\boldsymbol{r}) \tag{3.5}$$

for an atom in an optical lattice. Here $s(\boldsymbol{r}) = \frac{I(\boldsymbol{r})/I_s}{1+(2\delta/\Gamma)^2}$ is the saturation parameter. The eigenstates of the atom in the lattice are now given by the eigenstates of $H_{eff}(\boldsymbol{r})$ and are position dependent. In general each eigenstate is a superposition of Zeeman substates, only in the minima of the lattice is the eigenstate of the atom with the lowest energy equal to the Zeeman state $m_F = \pm F$ (for $\sigma^\pm$ polarization). The lattice potential

E_α for an eigenstate $|g_\alpha\rangle$ is given by

$$E_\alpha(\boldsymbol{r}) = \hbar\delta s(\boldsymbol{r})\lambda_\alpha(\boldsymbol{r})/2, \tag{3.6}$$

with λ_α the eigenvalue of Λ. In section 3.1.5 we will use the above to find the lattice potential for a ^{133}Cs atom on a $F = 4 \rightarrow F' = 5$ transition for the geometry of our optical lattice.

3.1.2 Sisyphus cooling

In 1988 Lett *et al.* surprisingly discovered that atoms in a MOT could be cooled below the Doppler limit [42]. This was followed quickly by the development of a theory of sub-Doppler cooling by Dalibard and Cohen-Tannoudji [43] and independently by the group of Chu [44]. The most common cooling mechanism was coined Sisyphus cooling as it described atoms continually climbing potential hills, similar to Sisyphus rolling his rock up a mountain.

We consider a one-dimensional optical lattice formed by counterpropagating laser beams with perpendicular linear polarizations, the so-called lin⊥lin configuration. Now the ellipticity of the polarization of the light field changes as a function of the position z along the lattice. If at $z = 0$ the polarization is σ^+ then at $z = \lambda/8$ the light will be π-polarized and at $z = \lambda/4$ it will have changed to σ^-. Sub-Doppler cooling occurs only if the atom has multiple Zeeman sublevels, so here we consider an atom on a $J_g = \frac{1}{2} \rightarrow J_e = \frac{3}{2}$ transition (the simplest atomic transition that gives rise to Sisyphus cooling). The atom experiences a sinusoidal potential when travelling through the lattice,

$$U_\pm(z) = \frac{1}{3}\hbar\delta s_0[2 \mp \cos(2kz)], \tag{3.7}$$

where $U_\pm$ denotes the potential for the $|g, +\frac{1}{2}\rangle$ and $|g, -\frac{1}{2}\rangle$ substates respectively and s_0 is the on-resonance saturation parameter [27]. The minima and maxima are located at the points of circular polarization. If the atom is in the $|g, +\frac{1}{2}\rangle$ substate it will see the sites with σ^+ polarization as minima and the ones with σ^- as maxima (due to the different Clebsch-Gordan coefficients for those transitions). Due to the position-dependent polarization of the light, the scattering rate of photons by an

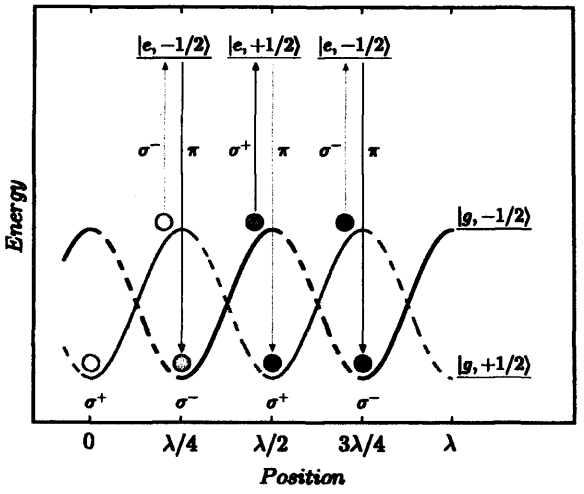

Figure 3.1: Illustration of the principle of Sisyphus cooling for an atom with $J_g = \frac{1}{2} \rightarrow J_e = \frac{3}{2}$ in a lin⊥lin optical lattice. The atom travels from left to right through the lattice and its energy is indicated by its colour (darker is less energetic). The up arrows denote absorption of a photon, the down arrows spontaneous emission.

atom depends on position as well and is given by [41]

$$\gamma_{\pm} = \frac{\Gamma s_0}{9[1 + (2\delta/\Gamma)^2]}[1 \pm \cos(2kz)], \tag{3.8}$$

where the subscript of $\gamma_{\pm}$ indicates the polarization of the scattered light.

Cooling occurs because the light pumps the atoms to the substate where the potential is lowest. So if we consider an atom in $|g, +\frac{1}{2}\rangle$ at a site with σ^+ polarization, it is at a minimum and will start to climb a potential hill. When it reaches the top of that hill the light polarization has changed to σ^- and the atom will be pumped to the $|g, -\frac{1}{2}\rangle$ state. Then it starts climbing the next potential hill till it reaches the top and gets pumped back again to the original $|g, +\frac{1}{2}\rangle$ state. This way it continually exchanges kinetic for potential energy, and this potential energy gets dissipated by the light field in the absorption - spontaneous emission cycles. An illustration of the mechanism of Sisyphus cooling is shown in figure 3.1.

3.1.3 Atom localization

One of the defining characteristics of optical lattices is their ability to trap atoms in a potential with long-range spatial order. This means that atoms can become localized near the, regularly distributed, potential minima. Atom localization was first observed in 1990 by Westbrook *et al.* [45]. This was done by measuring the fluorescence spectrum of atoms in a 3D optical molasses. The spectrum showed a central Dicke narrowed peak[1] on top of a Doppler-broadened background, a clear indication of atom localization. However, because six laser beams were used to form the molasses, the topography of the interference pattern changes as the relative phase between the beams drifts.[2] Therefore no long-range spatial order was observed in this experiment. The first real, one-dimensional, optical lattice was created by Verkerk *et al.* [48] two years later. The pump-probe spectroscopy technique described in section 3.2 was used to measure the spacing of vibrational levels in a potential well, and Bragg scattering showed the long-range order. Quickly thereafter, two other groups observed the same spectrum with spontaneous pump-probe spectroscopy [49] and in a two-dimensional lattice [50] respectively.

3.1.4 Umbrella lattice

The optical lattice structure we are using is the so-called *umbrella* lattice [51]. It consists of four linearly polarized laser beams, one of which propagates in the z direction while the other three beams propagate along the edges of a triangular pyramid. The azimuthal angle between beams $2-4$ is equal to $2\pi/3$, and we choose the polar angle between beam j, with $j = 2-4$, and the z-axis to be $\theta = \pi/6$. The relative intensities of the beams are $I_1 = 1$, $I_2 = I_3 = \sqrt{3+\cos^2\theta}/6\cos\theta$, $I_4 = 1/3$. The linear polarization of beam j is chosen as $\boldsymbol{\varepsilon}_j = \frac{\boldsymbol{k}_1 \times \boldsymbol{k}_j}{\|\boldsymbol{k}_1 \times \boldsymbol{k}_j\|}$, i.e. $\boldsymbol{\varepsilon}_j$ is orthogonal to the plane defined by $\boldsymbol{k}_1$ and $\boldsymbol{k}_j$ and oriented as shown in Fig. 3.2. The electric field amplitude of the umbrella lattice along the different basis vectors (3.1.1) is given by [51]

[1] R.H. Dicke showed in 1953 that the spectrum of an atom confined in a space comparable to the wavelength of the scattered light or smaller consists of a Doppler broadened part plus a narrowed central peak [46].

[2] An N-dimensional optical lattice is insensitive to phase drifts only if it is formed by $N+1$ laser beams [47].

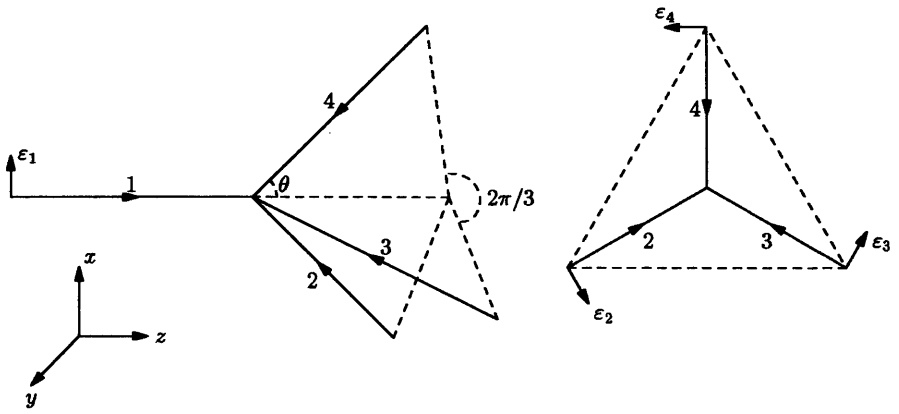

Figure 3.2: Laser beam configuration of the umbrella lattice. The numbers $1-4$ denote the beams and the vectors $\boldsymbol{\epsilon}_1 - \boldsymbol{\epsilon}_4$ the beam polarizations. On the left the viewpoint is indicated by the axes, on the right a projection on the xOy plane is shown.

$$E_{\pm}(r) = \frac{1}{\sqrt{2}} E_0 e^{-ikz} \left[\mp 1 + \frac{1}{3} e^{i(2k_{\parallel} z - k_{\perp} x)} + \frac{2}{3} \cos\left(\frac{1}{2}\sqrt{3} k_{\perp} y\right) e^{i(2k_{\parallel} z + k_{\perp} x/2)} \right]$$
$$E_z(r) = \frac{1}{\sqrt{3}} E_0 \tan\theta \sin\left(\frac{1}{2}\sqrt{3} k_{\perp} y\right) e^{-i(kz + k_{\perp} x/2)}, \qquad (3.9)$$

where $k_{\perp} = k \sin\theta$ and $k_{\parallel} = k\frac{1+\cos\theta}{2}$.

The choice for an umbrella lattice is made because beam 1 coincides with a symmetry axis of the lattice. This makes it straightforward to generate a force directed along this axis on the atoms by applying a phase modulation to beam 1. Note that the symmetry between the x- and y-axis is broken by the choice of polarizations described above.

3.1.5 Optical potential for caesium atoms

The structure of the optical potential for a ^{133}Cs atom on the $F = 4 \rightarrow F' = 5$ transition in the umbrella lattice described in the last section is non-trivial. The atom has nine eigenstates, each with its own optical potential that we can calculate by applying the theory of section 3.1.1. We obtain the polarization vector and amplitude of the light field from (3.9) and can then construct the light shift operator $\Lambda(\boldsymbol{r})$. There are now two different optical potentials we can obtain, the adiabatic and the diabatic

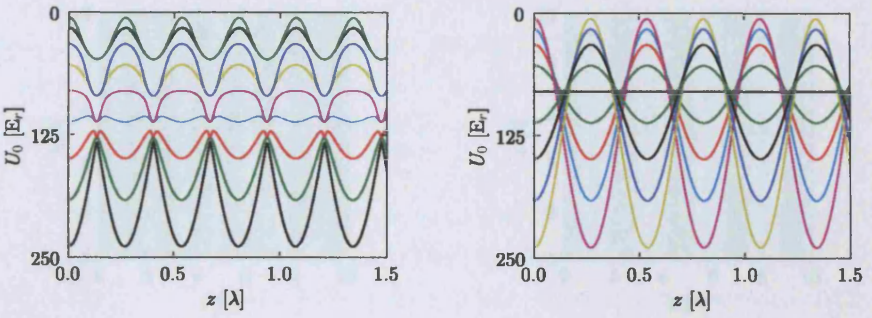

Figure 3.3: 1D potentials for ^{133}Cs on the $F = 4 \rightarrow F' = 5$ transition in the umbrella lattice (a) adiabatic potential. (b) diabatic potential.

potentials [41]. The adiabatic optical potential is calculated by diagonalizing $\Lambda(\boldsymbol{r})$ in the ground state Zeeman sublevels basis. The diabatic potential is calculated by keeping only the diagonal terms of $\Lambda(\boldsymbol{r})$ in that same basis. When used to find the potential depth, potential minima and vibrational frequencies, both potentials will give the same results. The difference between the two becomes important only when they are used for simulations with moving atoms. In that case the non-adiabatic motional couplings are usually neglected if the adiabatic potential is used, and the couplings contained in the non-diagonal elements of $\Lambda(\boldsymbol{r})$ are usually neglected if the diabatic potential is used [52]. In figure 3.3 we show both type of potentials along the z-axis of the umbrella lattice.[3] From now on we choose to only use the adiabatic potentials, as is usually done in the literature.

Even though there are $2F + 1$ potentials, the atoms spend the vast majority of their time in the deepest potential only, due to the optical pumping, as explained in section 3.1.2. So when we speak of *the optical potential* we mean the deepest of the $2F + 1$ potentials. To illustrate the topography of this potential we show cross-sections of it in figure 3.4. The potential minima are spaced by about $\lambda/4$ in the z-, 2λ in the x- and 2.3λ in the y-direction.

[3] We released the computer program *pyLattice*, capable of doing these calculations and 1D, 2D and 3D visualizations of optical lattices.

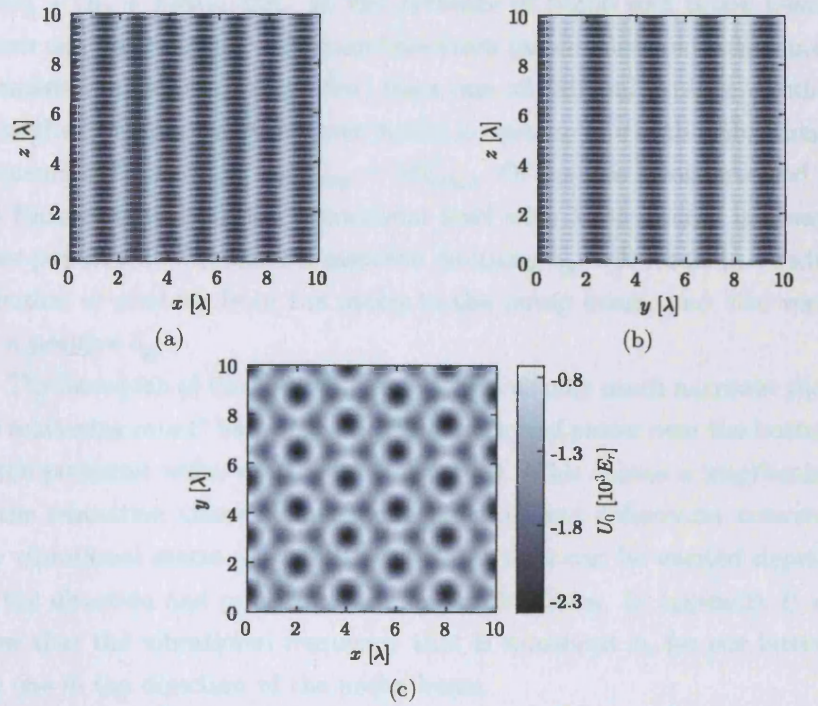

Figure 3.4: The lattice depth in the (a) xOz, (b) yOz and (c) xOy planes of the lattice, for an intensity of 50 mW/cm^2 and a detuning of $\delta = -12\Gamma$.

3.2 Pump probe spectroscopy

The optical lattice can be characterized efficiently by pump-probe spectroscopy. This entails measuring the transmission of a weak probe beam through the atom cloud trapped in the lattice, while the frequency difference between the probe and pump beams is scanned. In our case the probe beam frequency is kept constant while the frequency of the lattice beams, which act as pump beams, is ramped at a speed of 100 kHz/ms. A more common way is to keep the pump beam frequency constant and vary the probe beam frequency, but as long as the influence of varying the frequency of the lattice beams on the trapping potential is negligible both methods are equivalent.

The atoms are localized near the bottom of the (harmonic) wells and are thus well described as 3D harmonic oscillators with vibrational states $|n\rangle = |n_x, n_y, n_z\rangle$, with corresponding energies $E_n = (n_x + \frac{1}{2})\hbar\Omega_x + (n_y +$

$\frac{1}{2})\hbar\Omega_y + (n_z + \frac{1}{2})\hbar\Omega_z$ [53]. In the presence of pump and probe beams atoms can now undergo a Raman transition (absorption and subsequent stimulated emission of a photon) from one vibrational level to another when the detuning between these beams is equal to one of the vibrational frequencies, $\delta_{pp} \equiv \omega_{probe} - \omega_{pump} = \pm\Omega_{x,y,z}$. Of the two levels involved in the Raman transition, the vibrational level with lower energy is always more populated. Therefore a negative detuning δ_{pp} will result in a redistribution of photons from the probe to the pump beam, and vice versa for a positive δ_{pp}.

The linewidth of the Raman resonances is usually much narrower than the scattering rate Γ' because of the localization of atoms near the bottom of the potential wells, the Lamb-Dicke effect. This causes a lengthening of the relaxation times of the populations of, and coherences between, the vibrational states [54]. The transitions that can be excited depend on the direction and polarization of the probe beam. In appendix B we show that the vibrational frequency that is measured is, for our lattice, the one in the direction of the probe beam.

A typical spectrum is shown in figure 3.5. Two resonances at a pump-probe detuning $\delta_{pp} = \pm\Omega_v$ can be seen. These are Raman resonances, the one at $-\Omega_v$ caused by absorption of a photon from a pump beam and subsequent stimulated emission into the probe beam. The vibrational frequency is half the distance between these peaks. In addition to the Raman resonances the spectrum shows narrower resonances around $\delta_{pp} = 0$. These are Rayleigh resonances, whose width is a measure of the cooling rate of the atoms in the lattice [55].

3.3 Temperature and cooling rate

Atoms in the optical lattice experience Sisyphus cooling, as described in section 3.1.2. The equilibrium temperature of this process depends only on the depth of the lattice potential, and the rate at which this equilibrium is approached depends on the damping coefficient. This section describes experiments we performed with Caesium atoms in an umbrella lattice aimed at measuring the equilibrium temperature and cooling rate as functions of the lattice parameters.

We can determine the temperature of the atoms in the lattice by

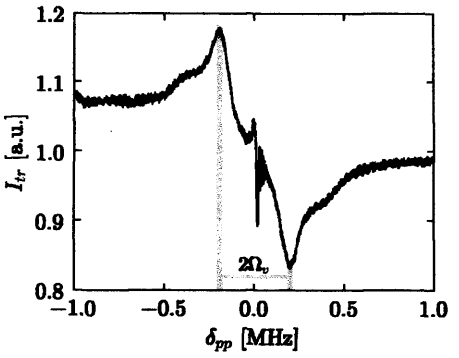

Figure 3.5: Pump-probe spectrum for a lattice with a detuning $\delta = -12\Gamma$. The vibrational frequency Ω_v along the z-axis is determined by measuring the distance between the two peaks, as indicated by the grey lines.

time-of-flight (TOF) imaging. After the atoms have been kept in the lattice for 20 ms, we turn the lattice off instantly and let the atom cloud expand ballistically for a time t_{exp}. The size of the cloud, determined by fitting a Gaussian profile to the image in the direction perpendicular to gravity, now depends on t_{exp} as

$$\sigma(t_{exp}) = \sqrt{\sigma_0^2 + \frac{k_B T}{m} t_{exp}^2}. \tag{3.10}$$

Here σ_0 is the initial size of the cloud, m the mass of a single atom and T the temperature we are interested in. We determine T by taking images for five values of t_{exp} and fitting (3.10) to the obtained cloud sizes. In figure 3.6 we show the cloud temperature as a function of potential depth for two different detunings.

Because the temperature for a given intensity I_z of lattice beam 1 in figure 3.6a is the same as that for $2I_z$ in figure 3.6b, we can conclude that T only depends on potential depth and is independent of the scattering rate. The approximately linear dependence of temperature on the lattice intensity - and therefore on the potential depth - is due to Sisyphus cooling, as illustrated in figure 3.1. Cooling stops when an atom does not have enough kinetic energy left to climb a potential hill to the point where it can lose energy by making a transition to a different internal state. Therefore the final temperature is a set fraction of the potential

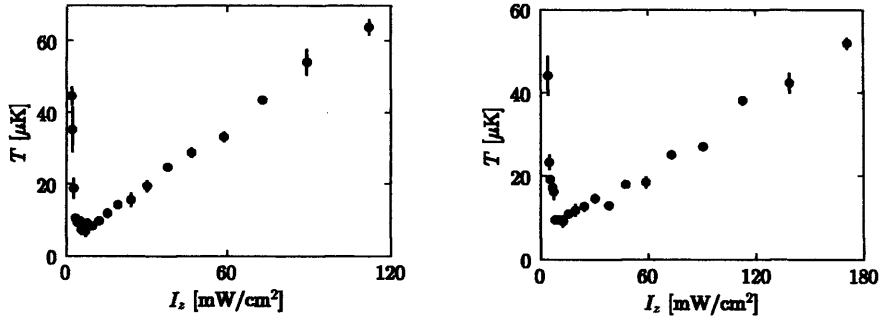

Figure 3.6: Temperature of the atoms in the lattice as a function of the intensity of the axial lattice beam. (a) lattice detuning is $\delta = -12\Gamma$ and $\Omega_v = 85 \pm 2$ kHz at $I_z = 60$ mW/cm^2. (b) $\delta = -24\Gamma$ and $\Omega_v = 85 \pm 2$ kHz at $I_z = 120$ mW/cm^2.

depth.

We also see that the minimum temperature of about 10 μK is reached for $I_z \simeq 7$ mW/cm^2 at $\delta = -12\Gamma$. For even smaller potential depths the so-called decrochage regime is reached. Here the potential is shallow enough to allow energetic atoms to travel over a distance of many potential wells without being trapped again. Therefore the temperature increases rapidly with decreasing potential depth in this regime. For larger potential depths the temperature increases approximately linearly with potential depth. These results are in good agreement with those in [56].

The temperature of atoms in an optical lattice has been investigated thoroughly before. Measuring the cooling rate, and thereby the damping coefficient γ, has proved to be a lot harder however. The only convincing experimental study reported in the literature to date measured the cooling rate by means of Bragg scattering of a weak probe beam. An inverse dependence on δ was found [57].

We measured the cooling rate by determining the temperature, with the same TOF method as above, as a function of the time t_{lat} the lattice is on. This gives an exponential decrease of temperature from the MOT temperature to the equilibrium lattice temperature, as shown in the inset

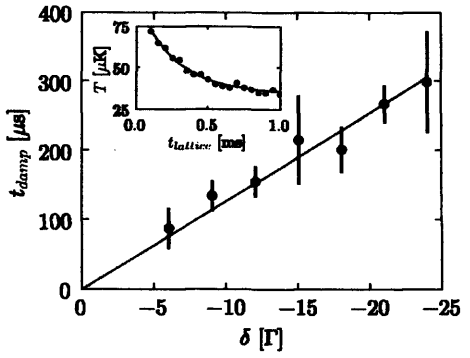

Figure 3.7: Damping time of the temperature in the lattice, measured along the z-axis, as a function of the detuning δ. The line is a least-squares fit to the data, constrained to go through the origin. The vibrational frequency of the atoms in the lattice is $\Omega_v = 70$ kHz. The inset shows the decrease of temperature as a function of the time the lattice is turned on for $\delta = -21\Gamma$.

of figure 3.7. We fit these curves with

$$T(t_{lat}) = (T_{MOT} - T_{eq})e^{-t_{lat}/t_{damp}} + T_{eq}, \tag{3.11}$$

and so obtain the damping time t_{damp}, which is inversely proportional to the damping coefficient. This damping time is shown in figure 3.7 as a function of δ for constant lattice depth. The lattice depth scales as $U_0 \sim I/\delta$ and the scattering rate as $\Gamma' \sim I/\delta^2$, therefore in figure 3.7 the detuning δ on the axis is proportional to $1/\Gamma'$. These results confirm clearly that the damping coefficient is proportional to the scattering rate.

Chapter 4

Ratchets

The history of ratchets goes back to the nineteenth century and is quite diverse, as outlined briefly in chapter 1 and in detail in [58]. In this chapter we will present an overview of the different type of ratchets and their characteristics with an emphasis on the work done since 1993, when Magnasco [9] 'reinvented' the ratchet, and on the theory that governs the behavior of cold atom ratchets.

4.1 Ratchet types

Many different types of ratchets have been proposed and implemented recently. We will focus here on the two most common types, flashing and rocking ratchets.

4.1.1 Flashing ratchet

The most basic ratchet in a way is the flashing ratchet [11, 12], where flashing refers to the potential turning on and off. The dynamics of particles in the ratchet potential $V(x)$ are governed by the Langevin equation

$$m\ddot{x} + \gamma\dot{x} = -V'(x)f(t) + \xi(t), \tag{4.1}$$

where γ is the damping coefficient, $\xi(t)$ is white noise ($\langle\xi(t)\rangle = 0$, $\langle\xi(t)\xi(s)\rangle = 2\gamma k_B T\delta(t-s)$) and $f(t)$ can only take on the values zero and one, turning the potential on and off.

The basic idea is shown in figure 4.1. Particles are located at the

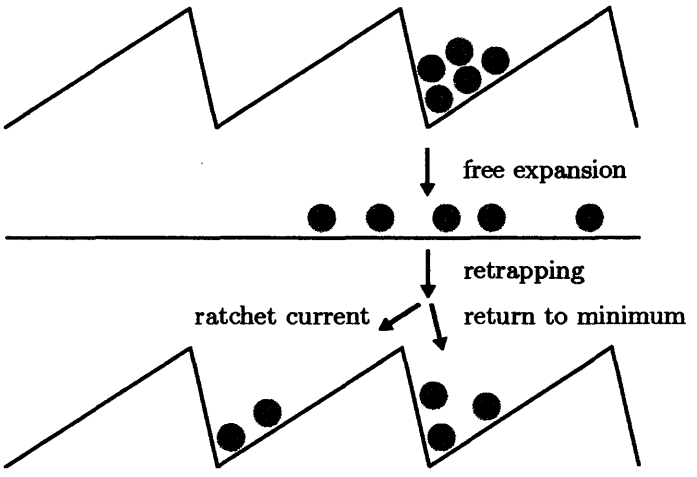

Figure 4.1: Schematic illustration of the operation of a flashing ratchet. Particles undergo normal diffusion when the potential is off, and return to a potential minimum when it is turned on again.

potential minima of an asymmetric potential, then when the potential is turned off they undergo normal diffusion. Due to the asymmetry of the potential more particles will reach the point where the maximum of the potential was located on the left than on the right. Thus when the potential is turned back on, those particles reach the neighboring minimum on the left. An average particle current to the left is obtained in this way. The operation of the flashing ratchet is straightforward, the particle current is in the direction of steepest ascent of the potential and work is done on the particles when turning the potential on, enabling the occurrence of a current.

Parrondo's game

A mathematical paradox designed to illustrate the often counterintuitive working of ratchets was designed in 1996 by Parrondo [59]. He proposed to play two gambling games, both losing on average, in an alternating way. He then showed that the result was a gain in capital no matter if the games were alternated regularly or at random. The design of the games is shown in figure 4.2. In game A a coin is tossed that has a probability $p_1 = 0.5 - \varepsilon$ to win and $1 - p_1$ to lose, with ε a small number. In game B a coin is tossed as well, but now with the probabilities determined by the

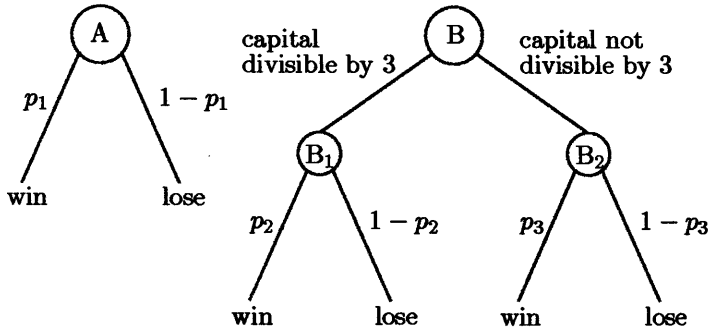

Figure 4.2: Schematic illustration of the original Parrondo's game. Games A and B are played a set number of times each or randomly alternating. Each game by itself loses on average, but combined they win.

capital of the player. If the capital is divisible by three the probability of winning is $p_2 = 0.1 - \varepsilon$, otherwise it is $p_3 = 0.75 - \varepsilon$. It can easily be shown that both games are losing on average when $\varepsilon > 0$.

Playing both games in an alternating order increases the player's capital, a result that can be understood by considering the equivalent flashing ratchet of figure 4.1. Game A is equivalent to the *off* state of the ratchet, with ε representing a slight tilt of the potential, and game B represents the *on* state [60]. The results of a numerical simulation of the Parrondo game are shown in figure 4.3. Both alternating strategies result in an increase of capital while playing either game by itself loses capital.

4.1.2 Rocking ratchet

The ratchet that is implemented in most experimental realizations is the rocking ratchet. Here the potential is constant and the atoms are driven with a zero-average periodic force $E(t)$. The dynamics are described by a Langevin equation of the form

$$m\ddot{x} + \gamma\dot{x} = -V'(x) + E(t) + \xi(t). \tag{4.2}$$

The term tilting ratchet is also used for this type of ratchet, because the driving force can be represented as a fluctuating macroscopic gradient or tilt of the potential. The operation of a rocking ratchet is shown

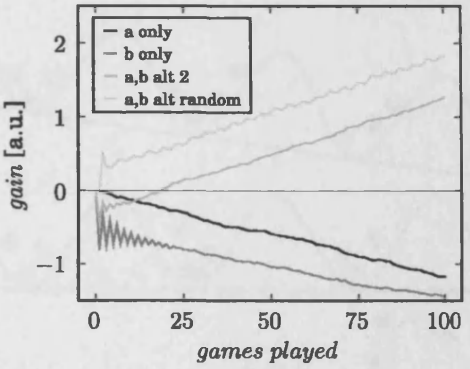

Figure 4.3: The gain when playing Parrondo's game as a function of the number of games played. Parameter values are $p_1 = 0.5 - \varepsilon$, $p_2 = 0.1 - \varepsilon$, $p_3 = 0.75 - \varepsilon$ and $\varepsilon = 0.005$.

schematically in figure 4.4. The 'natural' current direction is here in the opposite direction to that for the flashing ratchet, along the flattest slope of the potential.

When the driving is non-adiabatic, i.e. the period of $E(t)$ is not large compared to the characteristic time of the system, the rocking ratchet exhibits complicated behavior. The magnitude and even the sign of the current are unpredictable, and current reversals can occur as a function of driving parameters or noise strength. In contrast to the flashing ratchet, a current can also appear in a (noiseless) Hamiltonian system.

The cold atom ratchets that are the subject of this thesis are rocking ratchets driven in a non-adiabatic way. The basic picture of the operation of these ratchets is therefore as in figure 4.4, with the asymmetry contained in the driving force $E(t)$ and not in the potential $V(x)$. There are many other ways in which ratchets can operate, the common elements of which are (i) a mechanism to drive the system out of equilibrium and (ii) a way to introduce an asymmetry into the system. Ways to do this include entropic barriers [61], tunneling through barriers [19] and collective effects [62]. We will give a brief overview of experimental implementations in section 4.6.

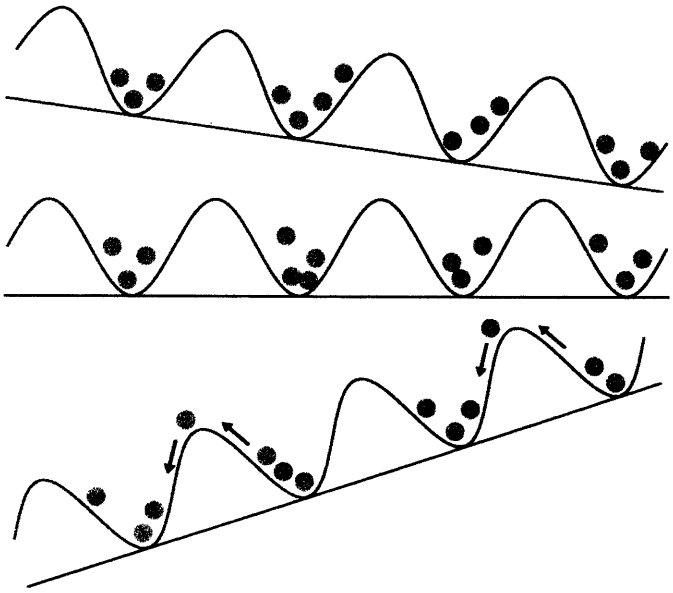

Figure 4.4: Schematic illustration of the operation of a rocking ratchet. The slope of the potential changes due to the asymmetric applied force $E(t)$. Here the potential is tilted slightly to the right for a large part of the driving period, and tilted strongly to the left for a much shorter time. The time-average of the applied force is zero, but due to the asymmetry of the force directed transport can occur.

4.2 Symmetries

Besides the requirement of driving the system out of equilibrium, a ratchet needs some kind of asymmetry to be able to operate. That a current occurs when the system does not possess any symmetry follows from Curie's symmetry principle, which states that if a certain phenomenon is not ruled out by symmetries then it will occur [58]. Symmetry analysis is therefore a powerful tool to predict where a current will or will not appear. Note that a system in thermal equilibrium always possesses a symmetry, namely that of *detailed balance*.

Symmetry analysis is based on finding conditions under which contributions to directed transport from particles with different initial positions and momenta cancel each other out. We therefore look for transformations of time and space that keep the equation of motion, i.e. the Langevin equation, invariant, while changing the sign of momentum $\dot{x}$. This means that if there is a certain probability of finding a particle with

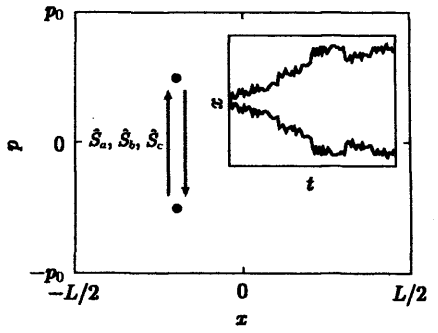

Figure 4.5: Schematic representation of the effect of symmetries (4.3) on trajectories in phase space. Two different trajectories are related by symmetries, whose contributions to directed transport therefore cancel each other. The inset shows a space-time representation of two related trajectories.

a trajectory $x(t, x_0, p_0), p(t, x_0, p_0)$ through phase space, the probability of finding another particle with a trajectory $x(t, x_0, -p_0), -p(t, x_0, -p_0)$ is equally large. Therefore the average momentum of a collection of particles, obtained by taking the average over many individual trajectories, will be zero. In figure 4.5 the linking of trajectories by symmetries is shown schematically.

There are two types of transformations that will yield the change in sign of momentum, these are (i) a change in sign of position, $x \to -x$, combined with a shift in time, $t \to t + t_0$, and (ii) a change in sign of time, $t \to -t$, combined with a shift in position, $x \to x + x_0$. When we apply these transformations to the Langevin equation (4.2), we find conditions on the driving force $E(t)$ and the potential $V(x)$ which have to be fulfilled for the Langevin equation to stay invariant. Adopting the notation of [63], the transformations with corresponding conditions are[1]

$$\begin{aligned} &\hat{S}_a : x \to -x, && t \to t + T/2, && \text{if}\{V_a', E_{sh}\}; \\ &\hat{S}_b : x \to x, && t \to -t, && \text{if}\{E_s, \gamma = 0\}; \\ &\hat{S}_c : x \to x + \lambda/2, && t \to -t, && \text{if}\{V_{sh}', m = 0\}. \end{aligned} \tag{4.3}$$

[1]For a periodic function $g(x)$ with period L there are three types of symmetry we consider here [63]. The function can be symmetric ($g(x) = g(-x)$), antisymmetric ($g(x) = -g(-x)$) and/or shift-symmetric ($g(x + L/2) = -g(x)$). We adopt the convention that symmetric functions are labelled with subscript s, antisymmetric functions with subscript a and shift-symmetric functions with sh.

Here $\gamma = 0$ indicates a dissipationless, or Hamiltonian, system and $m = 0$ indicates an overdamped system. Classification of systems as Hamiltonian, underdamped or overdamped shows which symmetries apply to that system, as well as what terms have to be retained in the Langevin equation. An atom in an optical lattice undergoing Sisyphus cooling can never be overdamped,[2] implying that for the experiments described in the next chapters only symmetries $\hat{S}_a$ and $\hat{S}_b$ are important.

4.3 Current reversals

Current reversals are a characteristic feature of ratchets. The interest in current reversals can be explained by the possibility to make devices that separate particles that possess different properties, like size [16] or mass [65].

Suppose we take a rocking ratchet with dynamics described by (4.2) and a symmetric potential $V(x)$. Then choosing an asymmetric driving $E(t)$ with amplitude F_0 will in general give us a nonzero current, as explained in the previous section. We can usually find a driving amplitude $F_1 \neq F_0$ where the current has opposite sign to that for F_0. Therefore there must be an intermediate amplitude F_2 where the current disappears, i.e. a current reversal occurs.

When we find a current reversal as a function of one parameter, it follows that a current reversal can occur as a function of any parameter of the system, for example the friction coefficient γ or the temperature T [58]. Say we found a current reversal at F_2, for a certain value of the friction coefficient γ_0. Then if we fix the driving amplitude at F_2 and start varying γ, a finite current will appear again. Generally the current as a function of γ will go through its zero point at γ_0 with a nonzero slope, therefore we will obtain a different sign of the current for $\gamma > \gamma_0$ than for $\gamma < \gamma_0$, demonstrating the current reversal at γ_0.

Multiple current reversals can occur for more complicated potentials or driving forces [66]. In chapter 5 we will see the occurrence of double current reversals in a cold atom ratchet as a function of several parameters.

[2]The damping coefficient saturates before the dynamics become overdamped, due to the saturation of the scattering rate when the intensity keeps increasing [64].

4.4 Ratchet performance

The interest in ratchets has largely been motivated by the prospect of new particle separation devices, electron pumps and microscopic motors. These are exciting prospects, but they are only realizable if their *energy efficiency* is acceptable, as first noted by Parrondo [67]. Another important requirement for these devices is reliability. As they are subject to fluctuations in their noisy environment, the work these devices do or the distances they travel in a fixed amount of time shows a spread [68]. Therefore we will define the *coherency* of a device as a second measure of performance.

4.4.1 Efficiency

The thermodynamic efficiency of a ratchet can be defined as the output work divided by the input energy,

$$\eta = \frac{W}{E_{in}}. \tag{4.4}$$

Since the ratchet has no internal degrees of freedom to store energy, the work can be defined as that done against a load force F [69],

$$\eta = \frac{F\langle v\rangle}{\dot{E}_{in}}, \tag{4.5}$$

where $\dot{E}_{in} = \langle \int_t^{t+T} v(t)E(t)dt \rangle$ is the time-averaged input power and $\langle v\rangle$ is the time-averaged velocity of the ratchet. This is the correct form for a thermodynamic efficiency, but many types of ratchets do not do work against an external force. Therefore Derényi *et al.* [70] proposed a generalized efficiency η_{gen} where the output work is defined as the minimum energy needed to perform a certain task. In many cases this is the energy $\gamma\langle v\rangle^2$ expended to move at an average velocity $\langle v\rangle$ through a viscous medium with damping coefficient γ, which makes η_{gen} equal to the Stokes efficiency [71].

An important next step was made by Suzuki and Munakata [72] who realized that the average power input must equal the average power out-

put, and can therefore be expressed in measurable quantities

$$P_{in} = F\langle v\rangle + \gamma\langle v\rangle^2 + \gamma(\langle \Delta v\rangle^2 - kT/m), \tag{4.6}$$

where $\langle \Delta v^2\rangle = \langle (v - \langle v\rangle)^2\rangle$ is the variance of the velocity. This enabled them to define a rectification efficiency

$$\eta_{rec} = \frac{F\langle v\rangle + \gamma\langle v^2\rangle}{F\langle v\rangle + \gamma\langle v\rangle^2 + \gamma(\langle \Delta v^2\rangle - kT/m)}. \tag{4.7}$$

This definition enables experimental determination of the rectification efficiency, by measuring (*i*) the average velocity $\langle v\rangle$, (*ii*) the variance of the velocity $\langle \Delta v^2\rangle$, (*iii*) the damping coefficient γ and (*iv*) the temperature T.

4.4.2 Coherency

The coherency of a ratchet defines how reliable the ratchet transport is. We consider here a ratchet that operates for a fixed time τ, and are interested in the distance $l = \langle v\rangle\tau$ travelled versus the spread in that distance. We define an effective diffusion constant [68]

$$D_{eff} = \frac{\langle x(\tau)^2\rangle - \langle x(\tau)\rangle^2}{2\tau}, \tag{4.8}$$

that enables us to quantify this spread. The Peclet number used in fluid dynamics gives us a useful measure of the coherency. It relates velocity to diffusion,

$$Pe = \frac{\langle v\rangle L}{D_{eff}}, \tag{4.9}$$

where L is a characteristic length scale of the system. In order to be able to compare ratchets of different size we choose L as the transport distance of the ratchet l. This choice gives us a Peclet number equal to

$$Pe = \frac{l^2}{\tau D_{eff}} = \frac{2l^2}{\langle \Delta x^2\rangle}, \tag{4.10}$$

which gives us a measure that can be determined experimentally. Coherent transport is usually taken as transport with a Peclet number of two or greater [73]. Experimentally the coherency has so far only been measured

in molecular motors, with Peclet numbers between two and six [74, 75]. Numerically it has been shown that there are regions of the parameter space where the coherence can be very large, with $Pe > 500$ [73].

When we look at the definition of the generalized efficiency (4.7) we can see that the coherency and efficiency are related, so when $\eta_{rec} \to 1$ then $Pe \to \infty$.

4.5 Microscopic dynamics

When we observe a ratchet current, this is usually a macroscopic averaged quantity that does not give us much information about the underlying microscopic dynamics of the system. Only in very simple cases such as the flashing ratchet from section 4.1.1 can we understand exactly how a macroscopic current arises from the microscopic dynamics. Symmetry considerations do not help us either in this respect. In this section we will take a closer look at the system dynamics on a single-particle level.

4.5.1 Stochastic dynamics

The dynamics of a single particle in a ratchet potential are described by a Langevin equation such as (4.2). To gain more insight into these dynamics we look at the phase space representation of the trajectories of single particles. We use a stroboscopic Poincaré section, created by plotting the position x and momentum p of each particle at multiples of the driving period T. The values for x are mapped to that of the unit cell of the periodic system, $-L/2 < x < L/2$.

We start by considering a Hamiltonian system by leaving out the white noise from (4.2) and using a potential $V(x) = -\cos(x)$, yielding a Langevin equation

$$m\ddot{x} = -\sin(x) + E(t). \tag{4.11}$$

We choose a driving force $E(t)$ with two harmonics and a phase difference ϕ between the two, $E(t) = E_1 \cos(\omega t) + E_2 \cos(2\omega t + \phi)$. This choice is made because it is a simple way of creating a periodic driving force that breaks all symmetries (4.3). It is also the same force we use for the experiments in chapters 5 and 6.

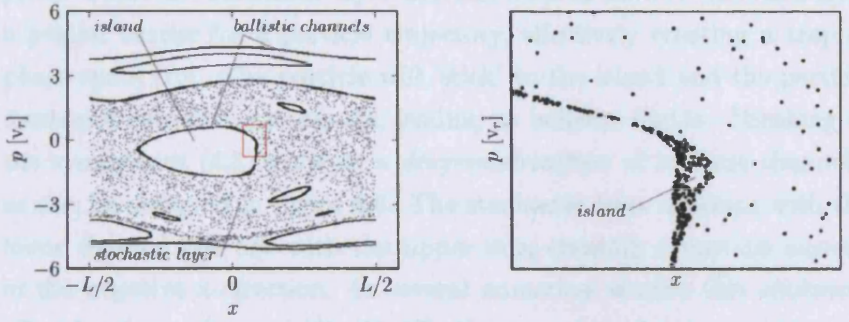

Figure 4.6: Result of numerical simulation of a system of the form (4.11). (*a*) Unit cell of the periodic system, with islands, ballistic channels and stochastic layer indicated. Average current is $\langle v \rangle = -0.21 v_r$. (*b*) Enlargement of area of figure *a* marked in red, showing the structure on the boundary of island and stochastic layer. Driving parameters are $E_1 = E_2 = 2$, $\omega = 2$ and $\phi = -\pi/2$, the mass m is taken as unity.

The phase space of (4.11) is characterized by the presence of a stochastic layer and is always mixed, i.e. it contains regular islands inside the stochastic layer. Regular islands with zero average momentum correspond to regular trapped motion of particles in the minima of the potential, islands with a nonzero average momentum to regular periodic motion. Outside of the islands, particles show chaotic motion. The layer also contains ballistic channels, particle trajectories that show long uni-directional flights [76].[3] In figure 4.6 we show the phase space representation of the results of a numerical simulation of (4.11), with islands, ballistic channels and stochastic layer identified.

The different parts of phase space in a Hamiltonian system do not communicate, i.e. particles that start inside a regular island stay inside that island and particles in the stochastic layer will exhibit chaotic motion for all time. The total current is then a sum of the currents for each part of phase space, weighted by phase space area, under the assumption that the particle dynamics is *ergodic*. Often this is not the case however, especially at the boundary between islands and the chaotic re-

[3]These are also known under the name Lévy flights, and have been observed in optical lattices [77].

gions. There the stochastic layer contains a set of *cantori*[4] that can form a partial barrier for a particle trajectory, effectively creating a trap in phase space [76]. The particle will 'stick' to the island and the particle dynamics becomes non-ergodic, leading to ballistic flights. Breaking of the symmetries (4.3) leads to a *desymmetrization* of ballistic channels, as can be observed in figure 4.6. The stochastic layer overlaps with the lower channel but not with the upper one, creating a particle current in the negative x-direction. In several numerical studies this *stickiness* effect has been observed [63, 76, 78]. However, in at least one numerical study it was shown that ballistic channels do not necessarily constitute the main contribution to the current [79].

For the Hamiltonian case the current is caused by a combination of ballistic flights and regular and chaotic transport. Now the question is what happens when noise is added to the system. In the presence of noise stable islands turn into *attractors*[5] with a corresponding basin of attraction. Particles can move into and out of these basins and the current depends on the attractors' stability properties [80]. The mechanism of ballistic channels generally survives in the presence of noise. It does not explain however that in some cases noise can play a constructive role and increase the current, as is demonstrated in chapter 5. For that we need to consider activated barrier crossing.

4.5.2 Activated barrier crossing

The escape of a particle from a potential well under the influence of thermal noise is a problem first treated by Kramers [81]. He showed that the escape rate out of the well depends exponentially on the barrier height, $W \sim e^{-U/k_BT}$, with U the barrier height, k_B the Boltzmann constant and T the temperature. When the particle is driven non-adiabatically this relation may be strongly modified. The escape rate is then modified and depends on an activation energy R different from the barrier height, $W \sim e^{-R/k_BT}$. Even if the driving amplitude, and thereby the change

[4]Cantori are KAM-tori - quasiperiodic orbits in phase space for integrable conservative dynamics - stable against perturbations.

[5]An attractor is a set to which the system evolves after a long enough time. This means a particle trajectory close to the attractor (in the basin of attraction) remains there even under a slight perturbation.

in R, is small, the escape rate can still be strongly modified as long as $\delta R > k_B T$. In [82, 83] it was shown that, counterintuitively[6], the change in R is proportional to the amplitude of driving A. The reason is that as a particle escapes from a well it follows with a very high probability a particular trajectory known as the optimal path [84]. Along this trajectory the effect of the driving field accumulates, causing a change in R linear in the field. The result is a logarithmic dependence of the escape rate on driving amplitude

$$\ln(W) = \chi(\omega)A, \tag{4.12}$$

with $\chi(\omega)$ a proportionality constant dependent on the frequency of driving called the logarithmic susceptibility. Like other susceptibilities, the logarithmic susceptibility is a characteristic of a system and can be calculated or measured experimentally. In [84] this was done for a colloidal particle in an optical trap. Crucially, it was shown that the escape rates to the left and right can have a different dependence on frequency, giving a mechanism of operation for a Brownian motor.

4.6 Experimental realizations of ratchets

Ratchets are systems that can operate when a few requirements are met, namely the system is described by Langevin dynamics away from equilibrium and the system contains an asymmetry. This means that a ratchet can be implemented in a multitude of ways, and over the last decade that is exactly what has been done. We will briefly describe two of the implementations, a complete overview of all ratchets to date is given in table 4.1.

The original inspiration for the recent interest in ratchets was the functioning of molecular motors [9]. Now Leigh and co-workers, in an impressive demonstration of nano-engineering, have been able to synthesize an artificial molecular device that works exactly like these molecular motors [21]. It belongs to a class of molecules known as rotaxanes, and consists of a molecular ring that is trapped on and can move along a

[6] One would expect the non-adiabatic driving to 'heat up' the particles and therefore the change in R to be proportional to the field intensity $I \sim A^2$.

Colloidal particle ratchet [16]	1994, sensitive to particle size
Optical thermal ratchet [17]	1994, flashing ratchet, single bead
Mercury in capillary [61]	1996, ratchet with entropic barriers
2DEG in antidot lattice [85]	1998, photo-voltaic effect
Cold atom ratchet [32]	1999, tailored optical lattice
Tunneling ratchet [19]	1999, works as electron pump
Quantum dot ratchet [86]	1999, adiabatic electron pump
SQUID ratchet [87]	2000, multiple current reversals
Magnetic flux ratchet [88]	2003, in superconducting film
Granular gas ratchet [89]	2004, collective ratchet
Josephson junction arrays [90]	2005, collective vortex ratchet
Self-propelled liquids [91]	2006, macroscopic effect on liquid
Collective vortex ratchet [62]	2006, multiple current reversals
Polymer nanowire ratchet [92]	2006, direction-dependent resistance
Synthetic molecules [21]	2007, first information ratchet

Table 4.1: Overview of experimental realizations to date of ratchets.

linear molecular thread. In the middle of the linear thread a molecular gate controls if the ring can pass to the other side or not. When light is falling on the ring, it can signal the gate to open if it is on one side but not on the other. This means the gate can act as a Maxwell's demon and increase the concentration of rings on one side, driving the whole system away from equilibrium. Note that the Second Law is not broken because energy is consumed when signalling the gate. See figure 4.7 for an illustration of the principle of this ratchet.

The first implementation of a ratchet with cold atoms in an optical lattice was done by Robilliard *et al.* [32]. There a magnetic field was used to create asymmetric lattice potentials for the two magnetic ground states in a Λ-configuration.[7] Due to the difference in asymmetry between these two potentials and the fluctuation-induced jumping of atoms between them, a large ($\langle v \rangle > 15 v_r$) rectification of fluctuations was obtained. The magnitude and direction of the atom current can be controlled by the magnetic field. In the last few years cold atoms, due to their flexibility and the precise control over all experimental parameters, have become one of the most interesting systems to study symmetries and transport

[7] A Λ-configuration consists of two ground states and one excited state. In this case it is obtained by using an atomic transition $F = 1 \rightarrow F' = 1$ and a light field containing no π-polarized component. The relevant magnetic substates are then $m_F = \pm 1$.

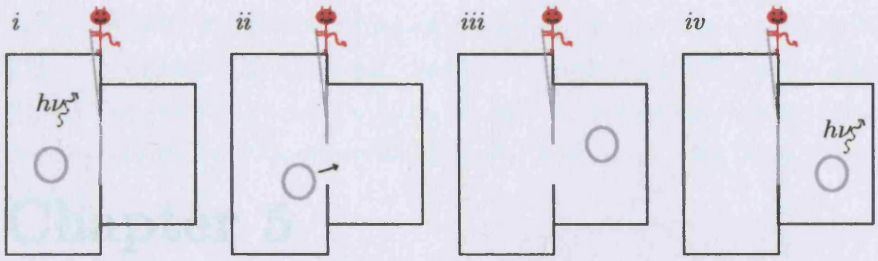

Figure 4.7: Illustration of the principle of the molecular information ratchet of Serreli *et al.* [21]. (*i*) Molecular ring signals the gate. (*ii*) Gate opens. (*iii*) Ring passes through the gate. (*iv*) Gate closes and the ring can not signal it anymore.

of ratchets [33–36, 93, 94].

Two patents related to ratchets have been awarded so far, the first one as far back as 1993 on a method to separate colloidal particles in fluids by means of a ratchet effect [95]. More recently, a method to reduce vortex densities and transport vortices in superconductors has been patented [20]. However, commercial exploitation of these patents has not happened yet as far as we are aware of.

Chapter 5

Ratchet transport mechanisms

This chapter describes an experiment that demonstrates resonant activation in a driven optical lattice:

- R. Gommers, P. Douglas, S. Bergamini, M. Goonasekera, P. H. Jones and F. Renzoni, *Resonant Activation in a Nonadiabatically Driven Optical Lattice*, Phys. Rev. Lett. **94**, 143001 (2005).

5.1 Introduction

Brownian motors function by extracting useful work out of fluctuations. An implementation of a Brownian motor with cold atoms in dissipative optical lattices was first shown by Jones et al. [94]. This work showed rectification of fluctuations, proving the ratchet functions as a Brownian motor. The underlying mechanism by which these Brownian motors operate was unclear however. Two closely related phenomena that use fluctuations constructively are *resonant activation* and *stochastic resonance*. In this chapter we will experimentally investigate transport in our ratchet in detail, and show that these phenomena both play a role in the regime where our ratchet acts as a Brownian motor. We will also find a regime of deterministic current rectification, namely *harmonic mixing*, and study the interplay between these different mechanisms.

Before discussing the above-mentioned phenomena, we would like to make clear that we now switch to a more experimentally oriented termi-

nology. We explicitly consider atoms in optical lattices, the dynamics of which are described by the same Langevin equations as in chapter 4. The white noise term $\xi(t)$ then becomes the photon scattering rate, and the damping coefficient γ is determined by the cooling rate due to Sisyphus cooling.

5.1.1 Resonant activation

We define resonant activation here as 'a resonant enhancement of the escape rate out of a potential well under the influence of non-adiabatic driving'. The resonant behavior occurs when the driving frequency matches a natural frequency of the undriven system, which for atoms in an optical lattice is the vibrational frequency Ω_v. It has been predicted that resonant activation causes resonant rectification of fluctuations [82, 83]. In an optical lattice we cannot observe the escape of atoms out of the potential wells directly, but we can observe any rectification of that escape. Therefore the observation of a resonance in the rectified atom current through the lattice is the hallmark of resonant activation for us.

Another possible consequence of resonant activation is the occurrence of current reversals. Resonant activation is an extra mechanism of rectification, and can give rise to a current with opposite sign to that from deterministic rectification - such as harmonic mixing, discussed in section 5.1.3. The interplay between these different mechanisms can give rise to current reversals. These reversals are interesting because of possible applications in particle separation, as discussed in section 1.1.4.

Resonant activation was first shown experimentally by Devoret et al. [96] in a Josephson junction driven by microwaves. The only other experimental demonstration that we are aware of was done with an optically trapped bead [84]. The work in this chapter, partially described in [33], will show resonant activation in a cold atom ratchet. In the literature we find another, closely related, phenomenon also named resonant activation [97]. In this paper thermally activated escape was considered in the presence of fluctuations of the barrier height itself, and a resonant escape behavior was found as a function of the barrier fluctuation frequency. Experimental demonstrations of this phenomenon were given with an analog electronic circuit [98] and with an optically trapped par-

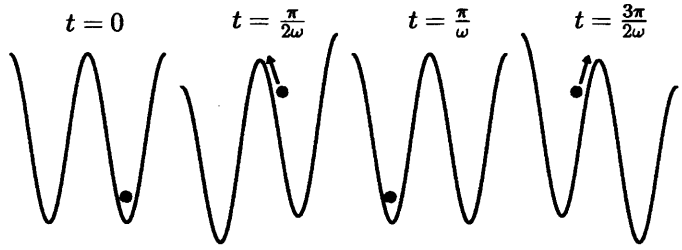

Figure 5.1: Schematic illustration of the principle of stochastic resonance in an optical lattice driven with a single harmonic $\sin(\omega t)$. The hopping rate of the atom shows a resonance when there is synchronization of the scattering rate with ω.

ticle [99]. We will not consider this phenomenon any further.

5.1.2 Stochastic resonance

In some cases an increase in noise on the input of a device can actually increase the signal to noise ratio at the output. This counterintuitive phenomenon is called stochastic resonance (SR). The mechanism of stochastic resonance is straightforward to explain. Consider an atom in an optical lattice that is driven with a single harmonic $\sin(\omega t)$, as shown in figure 5.1. The driving tilts the lattice so that the energy barrier between the two potential wells is decreased, increasing the probability of the atom making a (noise-induced) transition towards the well with lower energy. For this to happen repeatedly the driving frequency and the photon scattering rate need to be synchronized. Therefore the hopping rate of the atom between wells will show a maximum as a function of the scattering rate, i.e. stochastic resonance, when this synchronization occurs.

In general three ingredients are needed for SR to occur; (*i*) an energetic barrier, (*ii*) a weak coherent input and (*iii*) a source of noise. A very wide range of physical systems possess these characteristics, and SR can therefore be observed in systems ranging from a bistable ring laser [100] to neurons in the tail fan of a crayfish [101]. SR was originally proposed in 1981 by Benzi et al. [102] and used as an explanation for the periodical recurring of ice ages. Shortly afterwards Fauve and Heslot demonstrated SR experimentally by measuring the noise dependence of the spectral

line of an ac-driven Schmitt trigger [103].[1] A number of different measures have been used to characterize SR. The main ones are peaks in the intensity of a power spectrum, in a residence time distribution and in signal to noise ratio.

Stochastic resonance and resonant activation have often been studied separately, because the former occurs as a function of fluctuation intensity and the latter as a function of driving frequency. These two phenomena will often occur in the same system however, although not necessarily at the same points of the parameter space [99].

5.1.3 Harmonic mixing

Harmonic mixing [104, 105] is a deterministic mechanism for current generation that occurs if a particle confined by an anharmonic potential is driven by several commensurate frequencies. It can be viewed as a nonlinear process where the potential is the nonlinear medium that mixes the two (or more) harmonics of the driving field, resulting in a nonzero average momentum of the particle. Note that when a freely moving particle experiences this bi-harmonic driving, it will not exhibit directed motion because the time-averaged force is zero. A derivation of the directed current due to harmonic mixing for our potential and driving force is given by Flach et al. [106]. The current depends on the driving amplitudes E_1 and E_2 of the two harmonics, driving frequency ω and phase between the two harmonics ϕ,

$$J \sim \frac{E_1^2 E_2}{\omega^3} \sin(\phi). \tag{5.1}$$

We remark that this result for the harmonic mixing current comes from a perturbation approach under the assumptions of high temperature ($T \gg T_r$, with T_r the recoil temperature[2]) and strongly non-adiabatic driving ($\omega \gg \Omega_v$). These assumptions are only approximately correct and therefore we do not expect the scaling law (5.1) to hold exactly.

[1] A Schmitt trigger is a comparator circuit with positive feedback. With an input higher than a certain threshold the output is high, with an input below another (lower) threshold the output is low, and when the input is between the two thresholds the output does not change its value.

[2] The recoil temperature $T_r \equiv (\hbar k)^2/2k_B m$ is the lower limit of any cooling technique based on scattering of photons, and corresponds to the increase of kinetic energy of an atom after emitting a single photon. Equivalently, the recoil velocity is the velocity due to a single photon emission, $v_r \equiv \hbar k/m$.

Scaling laws under different assumptions can be found in [107]. Due to the strong dependence on ω, for driving frequencies low enough we expect deterministic rectification to be the dominant mechanism by which current generation occurs.

5.2 Experimental details

The experimental sequence consists of loading the MOT, cooling the atoms further by molasses, turning on the optical lattice, frequency modulating the lattice and then use fluorescence imaging to observe the effect of the modulation. Here we focus on the modulation of the optical lattice, the other steps are described in more detail in chapter 2. We generate the zero-mean force needed for the experiments by frequency modulating beam 1 of the optical lattice. This is done by modulating the frequency of the AOM controlling this beam (bottom left in figure 2.4). The force on the atoms is given by the inertial force in the accelerating frame $z' = z - \alpha(t)/k_z$, where $\alpha(t)$ is the phase modulation of the beam and $k_z = 2\pi/\lambda_z$, with $\lambda_z/2$ the separation between two minima of the lattice along the z-axis, $\lambda_z = \frac{\lambda}{1+cos(\theta)}$. The relationship between frequency and phase modulation is a differential one, $\omega(t) = \dot{\alpha}(t)$, or equivalently $\alpha(t) = \int \omega(t)dt$ [108]. The inertial force on an atom is now given by

$$E(t) = -ma(t) = -\frac{m}{k_z}\ddot{\alpha}(t). \tag{5.2}$$

We choose a bi-harmonic driving of the form

$$\dot{\alpha}(t) = \dot{\alpha}_0[\sin(\omega t) + 0.5\sin(2\omega t - \phi)], \tag{5.3}$$

with $\phi = \pi/2$ to ensure that symmetries $\hat{S}_a$ and $\hat{S}_b$ (4.3) are broken. This gives us a driving force

$$E(t) = \frac{m\omega^2\dot{\alpha}_0}{k_z}[\cos(\omega t) + \cos(2\omega t - \phi)]. \tag{5.4}$$

The frequency modulation for a few different phases ϕ is plotted in figure 5.2.

The modulation is turned on and off in an adiabatic way to avoid

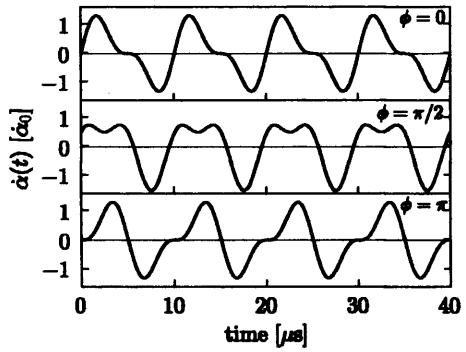

Figure 5.2: The shape of the waveform used for frequency modulation of beam 1 of the optical lattice, in case of bi-harmonic driving (5.3).

giving the atoms a sudden kick. This is achieved by multiplying the modulation amplitude with an envelope function

$$e(t) = \begin{cases} \frac{1}{2} + \frac{1}{2}\cos(\pi \frac{t-t_r}{t_r}) & ,0 < t < t_r, \\ 1 & ,t_r \leq t \leq t_r + t_e, \\ \frac{1}{2} + \frac{1}{2}\cos(\pi \frac{t-t_r-t_e}{t_r}) & ,t_r + t_e < t < 2t_r + t_e, \end{cases} \tag{5.5}$$

where t_r is the time of ramping up or down the modulation and t_e is the time the modulation is on. We always take $t_r = 1$ ms in our experiments, which fulfills the requirements of being fast on the timescale of the experiment ($t_r \ll t_e$) and adiabatic ($t_r \gg \omega^{-1}$). The envelope $e(t)$ is generated by the computer control program and multiplied with (5.3).

The fluorescence imaging gives us the position of the atoms at the moment of imaging. By comparing the images for finite $\dot{\alpha}_0$ with an image for $\dot{\alpha}_0 = 0$ we can determine the displacement of the atom cloud due to the applied force. We obtain the center of mass (CoM) displacement from the first moment of the image along the direction of motion,

$$d_{CM} = \frac{\sum_i \sum_j i I_{ij}}{\sum_i \sum_j I_{ij}}, \tag{5.6}$$

with I_{ij} the intensity of the image at pixel (i, j) and the atom cloud moving along image axis with index i. The motion of atoms through the lattice occurs with constant velocity, therefore we can obtain this velocity by simply dividing d_{CM} by the time t_e the experiment lasts. In all

experiments reported in this chapter we apply the frequency modulation for 20 ms, and let the atoms expand freely for another 20 ms. We checked that during the free expansion the atoms keep the same center of mass velocity as they have when the lattice is modulated. The free expansion therefore doubles the displacement of the cloud from its position without modulation, giving a better resolution of the measurement.

The center of mass velocity of the atoms depends on a number of parameters. The driving shape and amplitude are controlled by ω and $\dot{\alpha}_0$. The shape of the optical potential is fixed, but it's depth depends on the laser intensity and detuning. We characterize this depth by measuring the vibrational frequency Ω_v by means of pump-probe spectroscopy. The last parameter is the scattering rate, the rate at which a single atom scatters photons. This rate is represented here by $\Gamma_s = \Omega_v^2/\delta$, a quantity proportional to the scattering rate. We can change Ω_v and Γ_s independently, because $\Omega_v \sim I/\delta$ and $\Gamma_s \sim I/\delta^2$. The $\dot{\alpha}_0$'s given in the rest of this chapter are specified at $\omega = 100$ kHz. We change $\dot{\alpha}_0$ in such a way that the overall amplitude of the force is independent of ω.

5.3 Experimental results

5.3.1 Resonant activation and stochastic resonance

We measure the center of mass velocity of the atom cloud as a function of ω with driving of the form (5.3), for given lattice parameters Ω_v and Γ_s and driving amplitude $\dot{\alpha}_0$. In figure 5.3 we show data sets for three different scattering rates.

Each data set shows three different regimes. For low driving frequency ($\omega \ll \Omega_v$) harmonic mixing is the dominant effect. Due to the strong dependence[3] on ω in (5.1), harmonic mixing causes the velocity to be quite large. One thing we noticed is that in this regime the atoms diffuse quickly, and eventually the whole cloud breaks up for very small ω. We presume this is due to residual imbalances in the intensities of the optical lattice beams. In numerical simulations, where radiation forces always

[3]The assumptions under which (5.1) was derived do not hold in this regime, therefore the scaling with ω is not exact and for $\omega \to 0$ the current should disappear again.

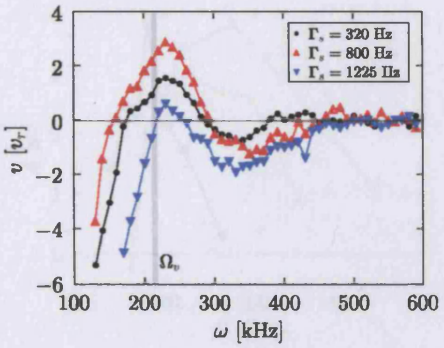

Figure 5.3: Atom current through the lattice as a function of driving frequency ω for different scattering rates Γ_s. The other parameters of the experiment are $\Omega_v = 214$ kHz and $\dot{\alpha}_0 = 750$ kHz at $\omega = 100$ kHz.

perfectly cancel, the ratchet velocity approaches zero in the limit of small ω [109]. For high driving frequency ($\omega \gg \Omega_v$) the current is essentially zero. Here the translations of the optical lattice in space that generate the driving force are so fast that the atoms cannot follow that motion and essentially see a potential averaged over a driving period. This stationary averaged potential does not allow for any current. The most interesting part of the data set is when the driving frequency approximately matches the vibrational frequency ($\omega \simeq \Omega_v$). There a resonance appears in the curve, corresponding to a resonant activation mechanism. We note that the maximum of this resonance appears to be at a frequency slightly higher than Ω_v. This is caused by the ω^{-3} dependence of harmonic mixing, which skews the shape of the resonance.

When we compare the three data sets we see that the current is highest for the intermediate value of Γ_s. This means that the scattering of photons plays a constructive role, i.e. fluctuations get rectified. This can be observed more clearly in figure 5.4, where we plot the maximum of the resonant activation resonance as a function of Γ_s for three different vibrational frequencies. The data in figure 5.4 for each Ω_v shows a resonant behaviour as a function of Γ_s. This is the hallmark of stochastic resonance, as discussed in section 5.1.2. So we find stochastic resonance and resonant activation occurring not only in the same system, but at the same point of the parameter space. We note that when rectification of fluctuations occurs, our ratchet acts as a Brownian motor. We con-

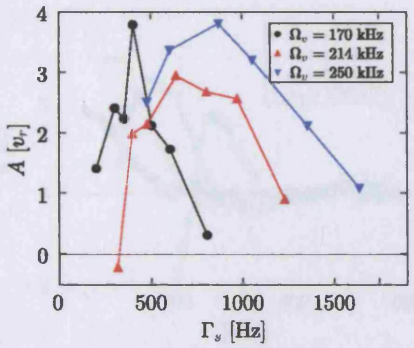

Figure 5.4: Amplitude of the resonant activation resonance as a function of the scattering rate Γ_s for three vibrational frequencies Ω_v. The driving frequency is $\dot{\alpha}_0 = 750$ kHz at $\omega = 100$ kHz.

clude that resonant activation is the underlying mechanism of the ratchet current if the ratchet is in the regime where it acts as a Brownian motor.

We now take a closer look at the build-up of the fluctuation-induced resonance. We take a single Ω_v and Γ_s and increase the driving amplitude from zero, where no rectification is expected, to the point where the resonance is most pronounced. The result is shown in figure 5.5. With no driving we do not get a ratchet current anywhere (data set not shown) and when we take a very small amplitude we get a current for low force. Then when we keep increasing the amplitude the current starts showing a current reversal and the resonance becomes more pronounced. We can't draw conclusions about why the current changes sign at a certain ω and $\dot{\alpha}_0$, as a complete theory for non-adiabatic driving is still missing.

Finally we can say something about the direction of the current. A current with positive sign means that atoms are predominantly hopping over the potential barriers when the force is large for a short time (see figure 5.2). Negative current means the opposite, there the force has opposite sign and is smaller but is applied for a longer time.

5.3.2 The complete parameter space

By repeating the measurements of figures 5.3 and 5.5 for different combinations of $\dot{\alpha}_0$, Ω_v and Γ_s, we can now explore the whole four-dimensional parameter space of our ratchet. The result is given in figure 5.6. The color indicates the velocity, where it is negative (indicated by blue) har-

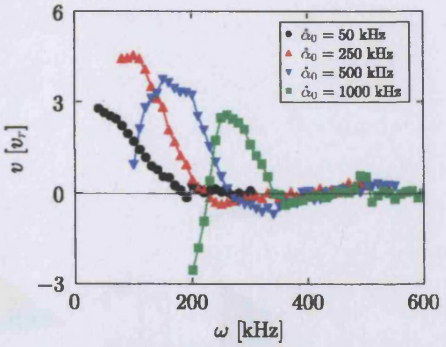

Figure 5.5: Atom current through the lattice as a function of driving frequency ω for driving strengths $\dot{\alpha}_0$. The other parameters of the experiment are $\Omega_v = 214$ kHz and $\Gamma_s = 635$ Hz.

monic mixing is the dominant effect. Positive velocity (indicated by red) implies resonant activation, and the atom works as a Brownian motor.

The three figures for different Ω_v are qualitatively the same. Therefore the vibrational frequency is not a very important parameter when determining in what regime the ratchet operates. The frequency ω where the velocity is maximal in the resonant activation regime does not change with Γ_s, as evidenced by the vertical plane in figure 5.6. Over the range we can tune Γ_s it does not have a qualitative influence on the shape of the $v - \omega$ curves of figure 5.3. The amplitude of the driving however has a large effect on the position of this maximum, as can be seen from the diagonal orientation of the red area in the horizontal planes of figure 5.6. We can conclude that the critical parameters for the qualitative behavior of the cold atom ratchet are ω and $\dot{\alpha}_0$. To optimize the ratchet velocity in a certain region of parameter space Ω_v and Γ_s can be used. As ω and $\dot{\alpha}_0$ are by far the easiest parameters to change and the ones that can be controlled most accurately, this is quite an important conclusion.

To be complete we also give the ratchet velocity as a function of the driving amplitude $\dot{\alpha}_0$ for different driving frequencies. These data sets, shown in figure 5.7, have been measured independently of those in figure 5.5, but can in principle be obtained from that figure by taking vertical cross-sections through the different curves there.

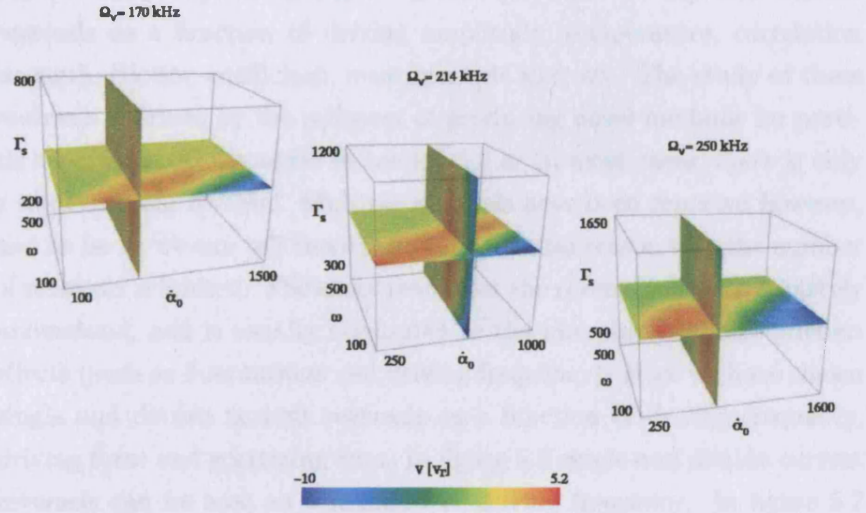

Figure 5.6: Ratchet velocity in four-dimensional parameter space. The color indicates the velocity, with red the regime of resonant activation and blue that of harmonic mixing. The driving amplitude $\dot{\alpha}_0$ and driving frequency ω are given in kHz, scattering rate Γ_s in Hz.

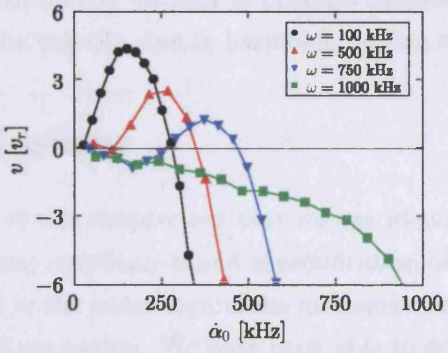

Figure 5.7: Atom current through the lattice as a function of driving amplitude $\dot{\alpha}_0$ for different driving frequencies ω. The vibrational frequency is $\Omega_v = 214$ kHz and the scattering rate is $\Gamma_s = 635$ Hz.

5.3.3 Current reversals

Current reversals can occur in ratchets when one of the control parameters of the ratchet is changed. In the literature we can find current reversals as a function of driving amplitude, temperature, correlation strength, friction coefficient, mass, particle size, etc. The study of these reversals is driven by the prospect of producing novel methods for particle separation, as discussed in section 1.1.4. In most cases, there is only a single current reversal. Multiple reversals have been reported however, and as far as we can tell there is no fundamental reason why the number of reversals is limited. The exact reason for the reversals is not completely understood, and is usually attributed to the interplay between different effects (such as fluctuations and driving frequency). Here we have shown single and double current reversals as a function of driving frequency, driving force and scattering rate. In figure 5.5 single and double current reversals can be seen as a function of driving frequency. In figure 5.7 single and double current reversals can be seen as a function of driving amplitude. And in figure 5.3 we can observe single current reversals as a function of scattering rate if we take vertical cross-sections through the figure (fixed ω).

The double current reversals can still be explained as being due to a single resonance only, on top of a harmonic mixing signal. The shift from single to double current reversals is due to a resonance amplitude large enough and a width narrow enough to produce ratchet velocities with a sign opposite to the velocity due to harmonic mixing at small ω.

5.4 Conclusions

The main results of this chapter are that we can identify the regimes of deterministic current rectification and of rectification of fluctuations, and that we show that in the latter regime the mechanism of operation of the ratchet is resonant activation. We have been able to explore a large part of the parameter space of our ratchet, and found that the parameters that determine in which of the two regimes the ratchet operates are the driving frequency ω and the driving amplitude $\dot{\alpha}_0$. Also, we have found current reversals as a function of several parameters.

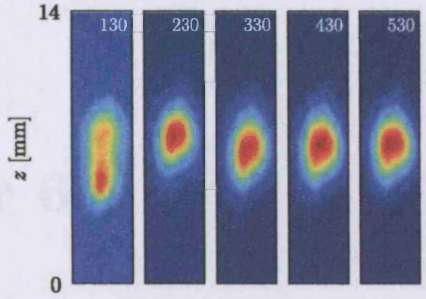

Figure 5.8: Fluorescence images for the data of figure 5.3. The images are labelled with the driving frequency ω. Scattering rate is $\Gamma_s = 800$ Hz and vibrational frequency $\Omega_v = 214$ kHz.

Numerical simulations of this ratchet have shown that the dynamical mechanism of operation of the ratchet in the case of deterministic rectification is the desymmetrization of islands and ballistic channels [80]. When the driving is symmetric a mixed phase space exists, but the stable islands and ballistic channels are located symmetrically with respect to $p = 0$. Choosing a phase $\phi = -\pi/2$ for the driving (5.3) causes this desymmetrization. A convincing microscopic explanation for the regime of rectification of fluctuations is still lacking.

An interesting open question is that of the efficiency and coherency of the ratchet in both regimes. Because we chose to let the atoms expand freely for 20 ms to increase the resolution of the measurement, it is not possible to get information on these quantities. The size of the cloud at the time of measurement is determined mainly by thermal expansion, obscuring information about the diffusion in the lattice. In figure 5.8 we show the fluorescence images for one of the data sets of figure 5.3. It can be seen that the cloud tends to break up for low ω, but other than that we can not tell if the ratchet acts coherently or not. We will address the coherency of the ratchet further in chapter 7.

Chapter 6

Dissipation-induced symmetry breaking

This chapter describes an experiment that demonstrates breaking of time-reversal symmetry by dissipation:

- R. Gommers, S. Bergamini and F. Renzoni, *Dissipation-Induced Symmetry Breaking in a Driven Optical Lattice*, Phys. Rev. Lett. **95**, 073003 (2005).

6.1 Time-reversal symmetry

We have observed directed motion following breaking the *temporal* symmetry of the system Hamiltonian in chapter 5. We can now ask if it is possible to break time-reversal symmetry for a symmetric Hamiltonian by means of dissipation alone.

The case of a cold atom ratchet with driving $\dot{\alpha}(t) \sim \sin(\omega t)+\sin(2\omega t+\phi)$ and negligible dissipation has already been investigated experimentally by Schiavoni et al. [110]. They found a $\sin(\phi)$ dependence of the atom current, consistent with what is expected when harmonic mixing is the only rectification mechanism. This implies that for a symmetric driving, i.e. $\phi = n\pi$ with n integer, no current is generated, in agreement with the symmetry considerations which hold in the Hamiltonian case. We aim now to understand how the picture is modified for a finite level of dissipation.

Numerical simulations [111] of the kinetic Boltzmann equation for an

ensemble of interacting particles with bi-harmonic driving showed that in the presence of weak dissipation the average particle current still shows a sinusoidal dependence on ϕ, but now with an extra phase shift

$$v_{max} \sin(\phi - \phi_0). \tag{6.1}$$

The phase shift was found to be an increasing function of the relaxation rate when the dissipation is small, and vanishes in the Hamiltonian limit. Therefore we take ϕ_0 as the signature of dissipation-induced symmetry breaking, and this is what we will measure experimentally. Note that we can only vary the lattice depth and detuning over a limited range[1], therefore we cannot completely suppress photon scattering. However, as we will see we can approach the Hamiltonian limit closely enough to make the phase shift disappear entirely. Therefore the lowest scattering rates in our experiment come close enough to the Hamiltonian limit to consider this limit a good approximation of the state of our system.

6.1.1 The fluctuation theorem

When we consider the microscopic dynamics of the atoms in the optical lattice, they are time-symmetric[2] even with dissipation present. This is seemingly at odds with time-reversal symmetry breaking by dissipation as contained in the Langevin equation, and even with the Second Law of thermodynamics. This discrepancy is known as Loschmidt's paradox. The fluctuation theorem [23, 113, 114] (FT) sheds some light on this paradox.[3]

The FT describes the probability distribution of entropy production for two classes of systems, those that start in equilibrium and those that are in a time symmetric nonequilibrium steady state. The FT is of the

[1] We employ two double pass AOMs before injecting the lattice slave laser, enabling us to change the detuning over the range -5Γ to -25Γ. We can vary Γ_s by a factor of four while keeping the lattice depth constant.

[2] This applies whether we take a classical or quantum view of the dynamics. For a discussion see [112, Chap. 27 – 30].

[3] There is actually a set of very similar fluctuation theorems, derived for different statistical ensembles. We here use the formulation by Crooks [113]. For an overview of the development of fluctuation theorems see [115]

form [113]

$$\frac{P_F(\omega_e)}{P_R(-\omega_e)} = e^{+\omega_e}. \tag{6.2}$$

Here ω_e is the entropy production of the system over some time interval, $P_F(\omega_e)$ is the probability distribution of that entropy production when the system is driven from some initial state A to a final state B, and $P_R(\omega_e)$ is the probability distribution when the system is driven from B to A in a time-reversed manner. This theorem is valid arbitrarily far away from equilibrium, and relates the probability of trajectories of the system with their reversed trajectories. From (6.2) we can conclude that the reverse trajectory becomes exponentially less likely to occur when the entropy production goes up. The microscopic dynamics are still time-reversible, therefore the FT is equally valid in reverse. It implies that a system moves from an ordered to a disordered state over time with overwhelming likelyhood. For the symmetry considerations in section 4.2 it means that the statistical weights of the trajectories as shown in figure 4.5 become unequal when dissipation is present, breaking time reversal symmetry.

6.2 Symmetries

We will now employ symmetry arguments to predict where the atom current will disappear. We do this for a symmetric potential and driving of the form

$$\dot{\alpha}(t) = \dot{\alpha}_0[\sin(\omega t) + 0.5\sin(2\omega t + \phi)]. \tag{6.3}$$

For any value of the damping coefficient γ the system possesses the symmetry

$$\hat{S}_a : x \to -x, \quad \phi \to \phi + \pi, \quad t \to t + T/2. \tag{6.4}$$

This means for the ratchet current J that $J(\phi) = -J(\phi+\pi)$, therefore the current only depends on odd harmonics of ϕ [80]. To go further we look at two limiting cases, the Hamiltonian and the overdamped case. The Hamiltonian case ($\gamma = 0$) additionally possesses time-reversal symmetry

$$\hat{S}_b : x \to x, \quad \phi \to -\phi, \quad t \to -t, \tag{6.5}$$

giving for the current $J(\phi) = -J(-\phi)$. Combining the two symmetries (6.4) and (6.5) gives

$$J(\phi) = J_1 \sin(\phi) + J_3 \sin(3\phi) + ... \tag{6.6}$$

The overdamped case ($m = 0$) possesses the extra symmetry

$$\hat{S}_c : x \to x + L/2, \quad \phi \to -\phi + \pi, \quad t \to -t, \tag{6.7}$$

giving for the current $J(\phi) = -J(-\phi + \pi)$. Combining again the two symmetries, (6.4) and (6.7), gives

$$J(\phi) = J_1 \sin(\phi + \frac{\pi}{2}) + J_3 \sin(3\phi + \frac{\pi}{2}) + ... \tag{6.8}$$

In practice we will find that $J_1 \gg J_3$, therefore the current dependence on ϕ is approximately sinusoidal. The phase shift changes from $\phi_0 = 0$ in the Hamiltonian limit to $\phi_0 = \pi/2$ in the overdamped limit. In the intermediate regime between these two limiting cases a qualitatively similar current dependence on ϕ is expected, i.e. fluctuations can influence the amplitude and phase shift of the sinusoid but not its shape. This derivation of the $\sin(\phi)$ dependence of the current is based on symmetry arguments only. A more formal derivation, as discussed in section 5.1.3 on harmonic mixing, can be found in [106].

One assumption in this discussion is that we can determine the symmetry of $V(x)$ by looking at the deepest optical potential for the ground state of the atom only. For our experiment this is justified, all ground state potential are symmetric around the same point as are the excited state potentials. It is possible however to create optical lattices with ground and excited state potentials that are individually symmetric but around different points [116]. The formally correct way to determine the symmetries, taking a parity operator P and applying it to the complete Hamiltonian, $P^\dagger H P$, then reveals that the complete potential is asymmetric.

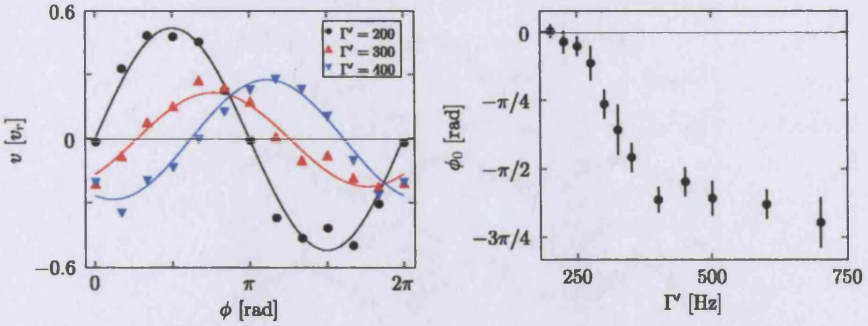

Figure 6.1: Demonstration of dissipation-induced symmetry breaking. (*a*) Ratchet current as a function of phase ϕ for three different scattering rates Γ_s. The solid lines are fits of (6.1) to the data. (*b*) Phase shift ϕ_0 of the ratchet current as a function of Γ_s. Other ratchet parameters are $\omega = 100$ kHz, $\Omega_v = 170$ kHz and $\dot{\alpha}_0 = 650$ kHz.

6.3 Experimental results

Our experimental setup is the same as the one described in section 5.2. The only difference is that we now apply the modulation for 30 ms and then let the atoms expand freely for 10 ms. The reason is that this decreases the atom cloud size at the time of imaging, while still providing the same displacement for the same average velocity. Due to the small ratchet velocity we averaged up to twenty images to get reliable results.

In figure 6.1a we show the ratchet current as a function of the phase difference ϕ between the two harmonics of the driving. For the lowest scattering rate the current is zero for $\phi = 0, n\pi$, for higher scattering rates it is clearly nonzero. We obtain the phase shift ϕ_0 by fitting these data sets with a function of the form (6.1). In figure 6.1b we show the magnitude of ϕ_0 as a function of the scattering rate. The phase shift is zero within the experimental error for the lowest two scattering rates, then it becomes an increasing function of the scattering rate. This shows the breaking of time-reversal symmetry by dissipation, and agrees quite well with the numerical simulations of [111]. It also agrees with our own numerical simulations, as published in [34].

In figure 6.2 the current as a function of ϕ and the associated phase shift are shown for each scattering rate. We can see that when the phase

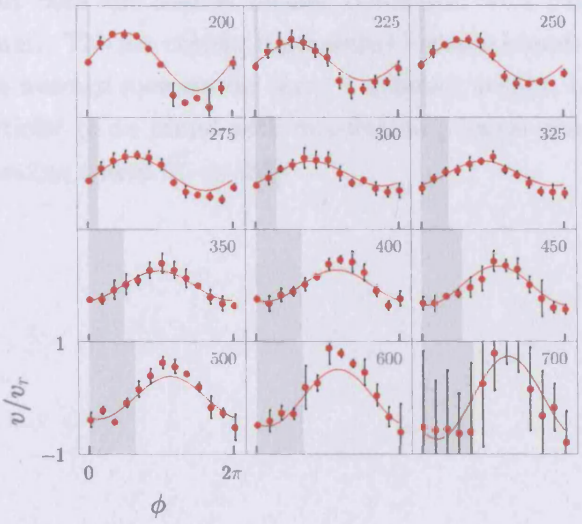

Figure 6.2: Ratchet current as a function of phase ϕ, for different scattering rates Γ_s. The solid lines are fits of (6.1) to the data. The phase shift ϕ_0 is indicated by the rectangular grey area.The lattice and driving parameters are the same as those for the data in figure 6.1a.

shift crosses $\pi/2$, i.e. when the current is zero when the temporal symmetry breaking is maximal, the amplitude of the fitted sine to the data becomes markedly smaller. A similar effect was observed in numerical simulations of our ratchet, a convincing explanation is still lacking however.

6.4 Conclusion

We have shown the transition from a parameter regime where the symmetries of the Hamiltonian system govern the existence of a ratchet current to a regime where dissipation causes a current in a ratchet with a completely symmetric Hamiltonian. Our result extends the theoretical approach of Yevtushenko et al. [111] from a system of interacting particles to a system where the dissipation is of a completely different origin.

The microscopic mechanism of rectification is slightly different as that for harmonic mixing described in section 5.4. Again the phase space

is mixed, but here the islands remain symmetric with respect to the momentum axis. The net current is generated because islands for positive and negative average momentum carry a different weight, i.e. an atom trajectory 'sticks' to an island with momentum p longer than it does to the corresponding island at $-p$ [80].

Chapter 7

Quasiperiodically driven ratchets

This chapter describes two experiments with quasiperiodically driven ratchets:

- R. Gommers, S. Denisov and F. Renzoni, *Quasiperiodically Driven Ratchets for Cold Atoms*, Phys. Rev. Lett. **96**, 240604 (2006).
- R. Gommers, M. Brown and F. Renzoni, *Symmetry and transport in a cold atom ratchet with multifrequency driving*, Phys. Rev. A **75**, 053406 (2007).

7.1 Introduction

The relationship between ratchet current and symmetry for periodic driving has been clearly demonstrated in the two previous chapters. Here we will extend the analysis to ratchets that are driven *quasiperiodically*. To that end we employ a multifrequency driving with components at frequencies ω_1, $2\omega_1$ and ω_2. When ω_2/ω_1 is irrational, the driving is quasiperiodic. In an experiment the ratio ω_2/ω_1 is always rational and can be expressed as p/q, with p and q two coprime positive integers. If p and q are sufficiently large, the driving can become quasiperiodic on the timescale of the experiment however.

We will investigate two different types of driving. The starting point is the bi-harmonic driving we used previously, $\dot{\alpha}(t) \sim \sin(\omega t) + 0.5\sin(2\omega t +$

ϕ). In the first case we then add a third driving frequency to these two. We will show that in the quasiperiodic limit the symmetries of the bi-harmonic driving are then restored. In the second case we multiply the bi-harmonic driving by a third frequency, which results in the complete suppression of current for all values of ϕ in the quasiperiodic limit.

7.2 Quasiperiodic symmetries

The relevant symmetries for the ratchet with bi-harmonic driving are $\hat{S}_a$ and $\hat{S}_b$, given in (4.3). When the driving becomes quasiperiodic these symmetries obviously do not apply anymore, as they were derived under the assumption of periodic driving. It was shown by Neumann and Pikovsky [117] that the periodic symmetries can be generalized by considering $\Psi_1 \equiv \omega_1 t$ and $\Psi_2 \equiv \omega_2 t$ as *independent* variables.

The driving force $E(t)$ is shift symmetric if it changes sign under any of the three transformations $\Psi_\alpha \to \Psi_\alpha + \pi$, with α any subset of $\{1,2\}$, i.e. the π shift is applied to any of the two variables or to both of them. If $E(t)$ is shift symmetric, the system is invariant under the transformation

$$\tilde{S}_a : x \to -x, \quad \Psi_\alpha \to \Psi_\alpha + \pi, \tag{7.1}$$

and no ratchet current will appear. Time-reversal symmetry can be generalized in the same way. The driving is symmetric if $E(-\Psi_1+\chi_1, -\Psi_2+\chi_2) = E(\Psi_1, \Psi_2)$, with χ_1, χ_2 constants. If $E(t)$ is symmetric then the system is invariant under the transformation

$$\tilde{S}_b : x \to x, \quad \Psi_\beta \to -\Psi_\beta + \chi_\beta, \tag{7.2}$$

with $\beta = (1,2)$. Again, no ratchet current will appear. We will now first investigate the case of additive quasiperiodic driving and see what the effect of $\tilde{S}_a$ and $\tilde{S}_b$ is.

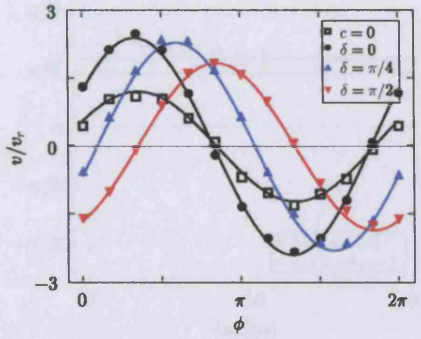

Figure 7.1: Ratchet current as a function of phase ϕ for bi-harmonic driving (□) and for additive quasiperiodic driving with three values of δ. The lines are fits of $v = v_{max}\sin(\phi + \phi_0)$ to the data. The driving frequencies are $\omega_1 = \omega_2 = 100$ kHz. Ratchet parameters are $\dot{\alpha}_0 = 75$ kHz, $a = b = c = 1$, $\Omega_v = 170$ kHz and $\Gamma_s = 460$ Hz.

7.3 Ratchet with additive driving

We employ the additive driving

$$\dot{\alpha}(t) = \dot{\alpha}_0[a\sin(\omega_1 t) + b\sin(2\omega_1 t + \phi) + c\sin(\omega_2 t + \delta)], \tag{7.3}$$

where we keep ω_1 at a fixed frequency of 100 kHz, and can vary the driving period $T = qT_1 = pT_2$ by adjusting $\omega_2 = p\omega_1/q$. We start by examining the case of bi-harmonic driving, i.e. $c = 0$. Again we measure the ratchet current as a function of ϕ and find a center of mass velocity $v = v_{max}\sin(\phi + \phi_0)$. The result is shown in figure 7.1 (black curve with □ markers). When we now introduce the third frequency, $c \neq 0$, with phase $\delta = 0$ and frequency such that $p/q = 1/1$ and measure the ratchet current as a function of ϕ, the amplitude of the curve has changed but the phase shift stays the same. Then when the phase δ is increased, an extra phase shift is measured and this phase shift is equal to $-\delta$. This is because for $\omega_2 = \omega_1$ and $a = b = c = 1$ the driving becomes

$$\dot{\alpha}(t) = \dot{\alpha}_0[2\cos(\delta/2)\sin(\omega_1 t) + \sin(2\omega_1 t + \phi - \delta)]. \tag{7.4}$$

To investigate the quasiperiodic limit we now keep δ fixed at $\pi/2$ and let pq, which we take as the measure of quasiperiodicity, go to infinity.[1]

[1]When we consider the common base period T_0 of both frequencies, then $T_1 = pT_0$

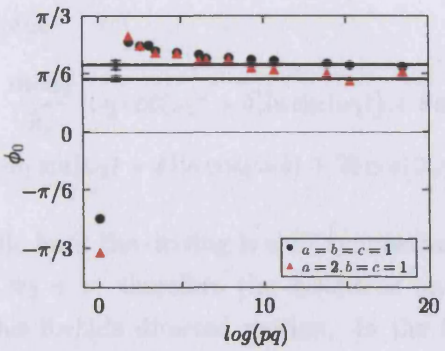

Figure 7.2: Phase shift ϕ_0 as a function of pq. Driving frequencies are $\omega_1 = 100$ kHz, $\omega_2 = p\omega_1/q$ and driving phase is $\delta = \pi/2$. All frequencies ω_2 used lie in the range 100−150 kHz. Ratchet parameters are $\dot{\alpha}_0 = 75$ kHz, $\Omega_v = 170$ kHz and $\Gamma_s = 460$ Hz.

In figure 7.1 we show the phase shift ϕ_0 as a function of pq for two different driving amplitudes. These results clearly show that in the limit of large pq the phase shift becomes equal to that for the bi-harmonic driving, indicated by the horizontal lines. This can be explained by considering the symmetries $\tilde{S}_a$ and $\tilde{S}_b$ which control the transport in the quasiperiodic limit. The shift symmetry $\tilde{S}_a$ is broken for any choice of ϕ and δ, and transport is controlled by $\tilde{S}_b$. The driving is invariant under the transformation $\Psi_2 \to -\Psi_2 + \chi_2$ for any δ, because δ can be absorbed in χ_2. Therefore the invariance under $\tilde{S}_b$ is determined only by the invariance of $E(\Psi_1, \Psi_2)$ under the transformation $\Psi_1 \to -\Psi_1 + \chi_1$, i.e. we recover the symmetry $\hat{S}_b$ which controls the transport in the case of pure bi-harmonic driving. In conclusion, in the quasiperiodic limit of additive driving the system recovers the behavior of the bi-harmonic, periodic driving.

7.4 Ratchet with multiplicative driving

We now switch our attention to a multiplicative driving of the form

$$\dot{\alpha}(t) = \dot{\alpha}_0 c \sin(\omega_2 t + \delta)[a \sin(\omega_1 t) + b \sin(2\omega_1 t)]. \tag{7.5}$$

and $T_2 = qT_0$. This means that the driving period T is equal to pqT_0, therefore pq is an appropriate measure of quasiperiodicity.

This results in a force

$$E(t) = -\frac{mc\dot{\alpha}_0}{k_z}\{\omega_2\cos(\omega_2 t+\delta)[a\sin(\omega_1 t)+b\sin(2\omega_1 t)] + \omega_1\sin(\omega_2 t+\delta)[a\cos(\omega_1 t)+2b\cos(2\omega_1 t)]\}. \quad (7.6)$$

In the quasiperiodic limit the driving is shift symmetric under the transformation $\Psi_2 \to \Psi_2 + \pi$, therefore the system is invariant under the symmetry $\tilde{S}_a$. This forbids directed motion. In the following, we will show experimentally that the current is zero if pq becomes large enough, as a result of the invariance under $\tilde{S}_a$. On the other hand, for periodic driving with p and q not too large we can expect nonzero currents if all symmetries are broken. In the next section we will examine the conditions under which this symmetry breaking occurs.

7.4.1 Symmetries

First let us consider the shift symmetry $\hat{S}_a$. Under the transformation $t \to t + T/2$ we have $\omega_1 t \to \omega_1 t + q\pi$ and $\omega_2 t \to \omega_2 t + p\pi$. It is straightforward to see that if q is even and p odd, symmetry $\hat{S}_a$ is satisfied. Therefore no current will be generated if q is even. If q is odd, directed transport is controlled by time-reversal symmetry $\hat{S}_b$. In the dissipationless limit $\hat{S}_b$ is realized if $E(t) = E(-t)$. We use this relationship to see when $\hat{S}_b$ is satisfied.

We start by taking only the first part of (7.6),

$$E(t) = \cos(\omega_2 t+\delta)\sin(\omega_1 t), \quad (7.7)$$

the second part of (7.6) will be used later. Now we assume $E(t)$ is invariant under time reversal at some time τ,

$$E(t+\tau) = E(-t+\tau). \quad (7.8)$$

After transforming $E(t)$ into single harmonics with the product formula $2\cos\alpha\sin\beta = \sin(\alpha+\beta) - \sin(\alpha-\beta)$ we end up with

$$\sin[(\omega_1\pm\omega_2)t+(\omega_1\pm\omega_2)\tau\pm\delta] - \sin[-(\omega_1\pm\omega_2)t+(\omega_1\pm\omega_2)\tau\pm\delta] = 0, \quad (7.9)$$

where $\pm$ indicates that this term occurs twice, once with all $+$ signs and once with all $-$. Using the sum formula $\sin(\alpha+\beta) = \sin\alpha\cos\beta + \sin\beta\cos\alpha$ to split this into t and τ dependent parts gives

$$2\sin[(\omega_1 \pm \omega_2)t]\cos[(\omega_1 \pm \omega_2)\tau \pm \delta] = 0. \tag{7.10}$$

Under time-reversal invariance this has to hold for all t, therefore

$$\cos[(\omega_1 \pm \omega_2)\tau \pm \delta] = 0. \tag{7.11}$$

Splitting the two equations gives

$$\begin{cases} \delta + (\omega_1+\omega_2)\tau = (n+\frac{1}{2})\pi, & n \text{ integer}, \\ -\delta + (\omega_1-\omega_2)\tau = (n'+\frac{1}{2})\pi, & n' \text{ integer}. \end{cases} \tag{7.12}$$

Subtracting and adding these two equations gives

$$\begin{cases} 2\omega_1\tau = (n+n'+1)\pi, \\ 2\delta + 2\omega_2\tau = (n-n')\pi. \end{cases} \tag{7.13}$$

Solving for δ and using $\omega_2/\omega_1 = p/q$ results in

$$\delta = -\frac{p}{q}(n+n'+1)\frac{\pi}{2} + (n-n')\frac{\pi}{2}. \tag{7.14}$$

We use $n_1 = n-n'$, $n_2 = n+n'+1$ and note that n_1 and n_2 have opposite parity. Now

$$q\delta = (qn_1 - pn_2)\frac{\pi}{2}. \tag{7.15}$$

We now use the second part of (7.6), $E(t) = \cos(\omega_2 t + \delta)\sin(2\omega_1 t)$, to obtain a second condition,

$$\cos[(\omega_1 \pm \omega_2)\tau \pm \delta + \omega_1\tau] = 0. \tag{7.16}$$

From (7.11) and (7.16) we see that $\omega_1\tau$ is a multiple of π or, equivalently, n_2 is even. With q odd and n_2 even we find from (7.15) that

$$q\delta = n\pi + \pi/2, \qquad \text{with } n \text{ integer}. \tag{7.17}$$

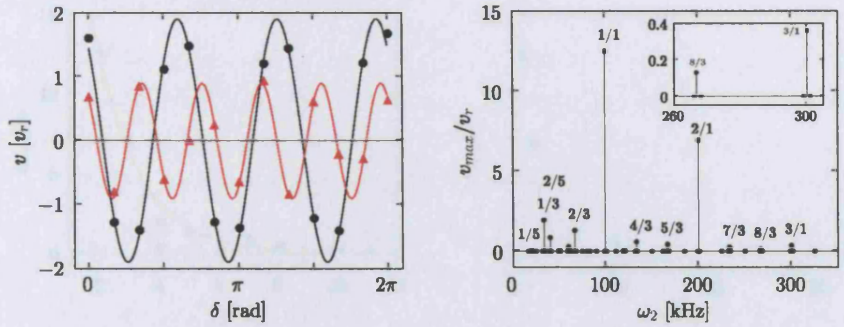

(a) (b)

Figure 7.3: Ratchet current for multiplicative quasiperiodic driving. (*a*) Current as δ is varied from 0 to 2π for ratio of driving frequencies $p/q = 1/3$ (•) and $p/q = 2/5$ (▲). The curves are fits of $v = v_{max}\sin(q\delta + \delta_0)$ to the data. (*b*) Amplitude v_{max} of sine curves from figure *a* as a function of driving frequency ω_2. Ratchet parameters are $\dot{\alpha}_0 = 300$ kHz, $a = 1$, $b = 0.5$, $c = 10$, $\Omega_v = 170$ kHz and $\Gamma_s = 460$ Hz.

We therefore expect a current dependence

$$J \sim \sin(q\delta - \frac{\pi}{2}). \tag{7.18}$$

When we now measure the ratchet current as a function of δ, as shown in figure 7.3a, we find q points where the current is zero. This is in excellent agreement with the dependence on δ (7.18) we expect from symmetry considerations. In figure 7.3b we show the amplitude v_{max} of fits of (7.18) to the data of figure 7.3a for a range of driving frequencies ω_2. The current is zero everywhere except at exactly those values of ω_2 where the ratio ω_2/ω_1 is rational with small p and q. We also see that we only get a current for q odd, as a result of the invariance of the system under $\hat{S}_a$ when q is even.

7.4.2 Higher order harmonic mixing

In section 5.1.3 we discussed the effect of mixing of two harmonics of frequency ω and 2ω by an anharmonic potential, which resulted in a current $J \sim \frac{E_1^2 E_2}{\omega^3}\sin(\phi)$. It is also possible however for harmonic mixing to occur for commensurate frequencies $p\omega_1 = q\omega_2$. In the high frequency

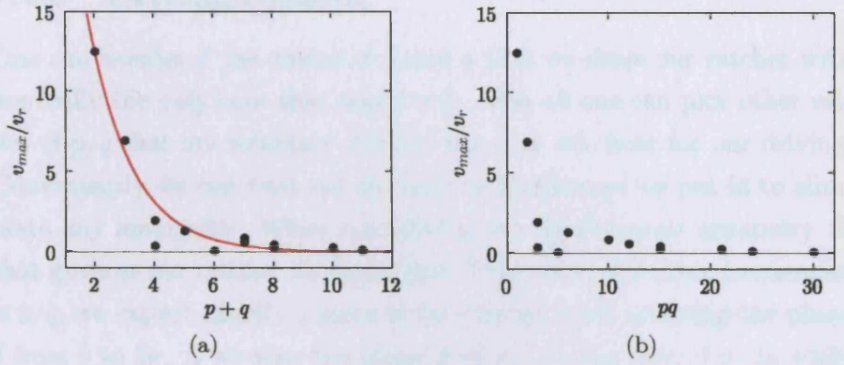

Figure 7.4: Amplitude of the ratchet current peaks. (a) as a function of $p+q$. The red line indicates the $p+q$ dependence expected from harmonic mixing, $v_{max} \sim (\frac{1}{2})^{p+q}$. ($b$) as a function of pq, which is our measure of quasiperiodicity. The ratchet parameters are the same as those in figure 7.3.

limit this gives a $(p+q)$th order rectification effect [118] for q odd,

$$J \sim \left(\frac{1}{2}\right)^{p+q} \left(\frac{E_1}{\omega_1}\right)^p \left(\frac{E_2}{\omega_2}\right)^q \cos(\Delta_{p,q}), \tag{7.19}$$

where $\Delta_{p,q} = q\delta - p\phi$ with ϕ and δ as in (7.5) is the higher order phase difference between the harmonics.

In figure 7.4a we have plotted the amplitudes of the maximal ratchet velocities of figure 7.3b as a function of $p+q$, as well as the expected decrease of this amplitude according to (7.19). Apart from a few outliers that are due to frequencies $\omega_2 \gg \Omega_v$, the amplitude drops off in accordance with (7.19), suggesting that harmonic mixing is the dominant rectification effect.

In figure 7.4b the same amplitudes are shown as a function of pq, our measure of quasiperiodicity. It is clear that in the limit of large pq the current goes to zero, due to the invariance of the system under symmetry $\tilde{S}_a$. These two explanations for the decrease in current are complementary. Symmetries determine where the current is zero, and harmonic mixing is the dominant rectification effect.

7.4.3 Driving readout

One can wonder if the values of p and q that we drive our ratchet with are really the only ones that play a role, after all one can pick other values of p/q that are arbitrary close to the ones we chose for our driving. Conveniently we can *read out* the ratio of frequencies we put in to eliminate any ambiguity. When considering the time-reversal symmetry $\hat{S}_b$ that governs our ratchet we found that if the ratio of driving frequencies is p/q, we expect exactly q zeros in the current when scanning the phase δ from 0 to 2π. If we scan the phase ϕ of our driving from 0 to 2π while keeping δ constant,

$$\dot{\alpha}(t) = \dot{\alpha}_0 c \sin(\omega_2 t)[a \sin(\omega_1 t + \phi) + b \sin(2\omega_1 t + 2\phi)], \tag{7.20}$$

we equivalently find exactly p zeros. This can be seen by making the transformation $t \to t - \phi/\omega_1$, we find a driving of the form (7.5) with $\delta = -\omega_2\phi/\omega_1 = -p\phi/q$. Therefore condition (7.18) for time reversal becomes

$$J \sim \sin(p\phi - \frac{\pi}{2}). \tag{7.21}$$

In figure 7.5 we demonstrate the readout of both p and q. It shows that the driving indeed determines p/q and that atom transport through the lattice is controlled by time-reversal symmetry.

7.4.4 Spectroscopy of a resonance line

When the frequency ω_2 is scanned around ω_1 we obtain a series of narrow lines, as shown in figure 7.3b. Here we address the question of the lineshape of a single line in that series, and its linewidth as a function of the interaction time. Consider a ratio of driving parameters p_0/q_0 that gives a nonzero current amplitude v_{max}. We indicate the corresponding frequency by $\omega_2^0 = p_0\omega_1/q_0$. We now scan ω_2 around this center frequency ω_2^0 and measure the current amplitude of a scan of δ.

We first consider the case $p_0/q_0 = 1/1$, and scan ω_2 in a range of about 200 Hz. The result is given in figure 7.6. For all frequencies in the range we find that the data is well fitted by $v = v_{max} \sin(q_0\delta - \pi/2 - \delta_0)$, therefore higher order driving parameters p/q corresponding to $\omega_2 \neq \omega_2^0$ do not contribute to the current or do so well below our experimental

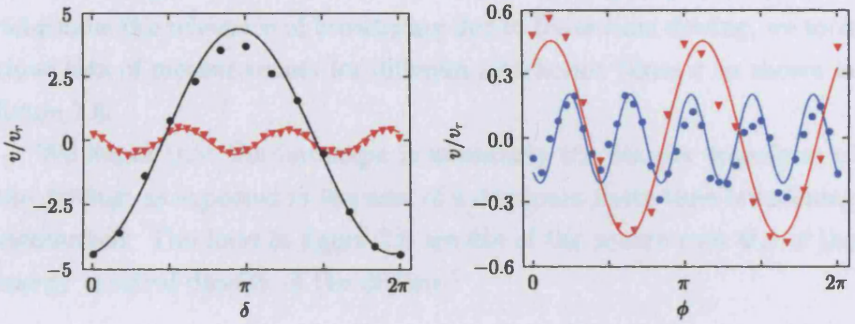

(a) (b)

Figure 7.5: Readout of the values of (a) q and (b) p, by measuring the ratchet current as a function of δ and ϕ respectively. The driving parameters are $\dot{\alpha}_0 = 100kHz$, $a = c = 1$, $b = 0.5$ and $\omega_1 = 75$ kHz. The red curves are for $p/q = 2/3$, the black one for $p/q = 1/1$ and the blue one for $p/q = 2/5$. The lines are fits of the data with $v = v_{max}\sin(q\delta - \pi/2 - \delta_0)$ and $v = v_{max}\sin(p\phi - \pi/2 - \phi_0)$ for figures a and b respectively. Parameters for the optical lattice are $\Omega_v = 124$ kHz and $\Gamma_s = 190$ Hz.

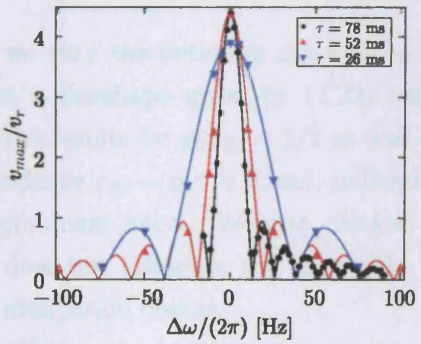

Figure 7.6: Spectroscopy of a resonance line. The current amplitude is given as a function of $\Delta\omega = \omega_2 - \omega_2^0$. Each data point is the amplitude v_{max} of a fit of $v_{max}\sin(q\delta - \pi/2 - \delta_0)$ to the ratchet current measured as a function of δ. The parameters of the driving are $\omega_1 = 75$ kHz, $\omega_2^0 = 75$ kHz (i.e. $p_0/q_0 = 1/1$, $\dot{\alpha}_0 = 100$ kHz, $a = c = 1$, $b = 0.5$. The lines are fits of the data with Φ_{sr} (7.22).

resolution. This suggests that the linewidth and lineshape are determined by broadening processes and not by driving with higher p/q. In order to determine the relevance of broadening due to finite-time driving, we took three sets of measurements for different interaction times τ as shown in figure 7.6.

We found that the lineshape is essentially the Fourier transform of the driving, as expected in the case of a dominant finite-time broadening mechanism. The lines in figure 7.6 are fits of the square root Ψ_{sr} of the energy spectral density of the driving,[2]

$$\Phi_{sr} = \Phi_0 \frac{2|\sin(\tau_{fit}\Delta\omega/2)|}{\Delta\omega}, \tag{7.22}$$

with Φ_0 a constant of proportionality and τ_{fit} equal to the interaction time τ. This is consistent with a simple dimensional analysis. The atomic kinetic energy and the power dissipated scale both with the energy introduced in the system via the driving, which is given by the energy spectral density. This corresponds to a scaling of the velocity with the square root of the energy spectral density.[3] For larger values of p_0/q_0 we found the exact same behaviour, with the relevant detuning $\Delta\tilde{\omega}$

$$\Delta\tilde{\omega} = q_0\omega_2 - p_0\omega_1. \tag{7.23}$$

In the experiment we vary the detuning $\Delta\omega = \omega_2 - p_0\omega_1/q_0 = \Delta\tilde{\omega}/q_0$, therefore we expect a lineshape given by (7.22) with $\tau_{fit} = q_0\tau$. In figure 7.7 we show the results for $p_0/q_0 = 2/3$ as well as for $p_0/q_0 = 1/1$. The expected dependence $\tau_{fit} = q_0\tau$ is found, indicating that finite-time broadening is the dominant effect. We also checked that changing the scattering rate Γ_s does not influence the linewidth, therefore no extra broadening due to dissipation occurs.

We note that in (7.6) we neglect the adiabatic turn on and turn off of $f(t) = e(t)E(t)$. e

[2]The energy spectral density is given by $\Phi(\Delta\omega) = |\frac{1}{\sqrt{2\pi}}\int_{-\infty}^{\infty} f(t)e^{-i\Delta\omega t}dt|^2$, with $f(t) = e(t)E(t)$.

[3]This is true for a single value of p_0/q_0. When scanning ω_2 over a much larger range, such as used in figure 7.3b, other factors such as the value of p_0/q_0 and how close ω_2 is to Ω_v have a strong influence on the amplitude of the ratchet current.

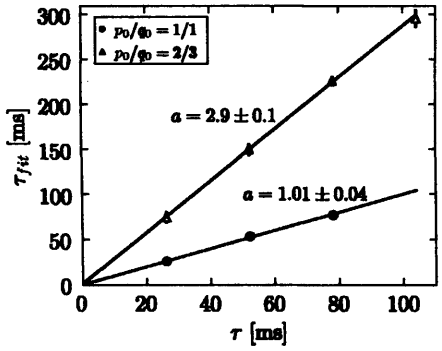

Figure 7.7: Fitting parameter τ_{fit}, as derived by fitting data as those of figure 7.6 with Φ_{sr}. The straight lines represent the best fit of the data with the function $\tau_{fit} = b + a\tau$, the result for a is given.

is given by

$$\Phi(\Delta\omega) = |\frac{2\sin(\Delta\omega\tau/2)}{\Delta\omega} + \frac{2\cos(\Delta\omega\frac{t_r+\tau/2}{2})\sin(\Delta\omega t_r/2)}{\Delta\omega} + \frac{\Delta\omega}{\Delta\omega^2 - (\pi/t_r)^2}\sin(\Delta\omega\frac{t_r+\tau/2}{2})\cos(\Delta\omega t_r/2)|^2. \quad (7.24)$$

Essentially this is the Fourier transform of a square pulse of time τ multiplied by a modulation with a period t_r^{-1} because of the adiabatic turning on and off of the driving. If the frequency range over which we scan $\Delta\omega$ is much smaller than t_r^{-1}, we can therefore approximate $\Phi(\Delta\omega)$ by Φ_{sr}. In our case $t_r^{-1} = 500$ Hz, and $|\Delta\omega| < 100$ Hz, therefore our data is well described by (7.22).

7.5 Coherency for multiplicative driving

In section 4.4 we introduced the Peclet number as a measure of coherency of the ratchet. It is defined as twice the center-of-mass displacement of the atom cloud squared divided by the variance of that displacement,

$$Pe = \frac{2l^2}{\langle\Delta x^2\rangle}. \quad (7.25)$$

Here we will determine the Peclet number for the multiplicatively driven ratchet with $p/q = 1/1$ and $p/q = 1/3$ of figure 7.3.

In figures 7.8a and 7.8b we show fluorescence images of the atom clouds immediately after the driven lattice has been turned off, for driving phases δ between 0 and π. It can be clearly seen that the separation between the clouds at maximum displacement is large enough for the clouds to not overlap. This indicates that the motion is coherent, i.e. the Peclet number is larger than two. In figures 7.8c and 7.8d we show the intensity profile along z of two of those fluorescence images. In all cases the profiles are described reasonably well by Gaussian distributions, indicating that the complete atom cloud is set in motion by the driving. We determine the displacement l and the square root of the variance $\sqrt{\langle \Delta x^2 \rangle}$ from the center and the variance of the Gaussian, and indicate these in the profiles. The Peclet numbers for these profiles are $Pe_{1/1} = 4.3 \pm 0.5$ and $Pe_{1/3} = 2.8 \pm 0.6$. These numbers are a slight underestimation of the real values, because we have neglected the initial size of the atom cloud.

The coherency of our ratchet is comparable to that of molecular motors found in nature. In numerical simulations very large coherencies have been observed, however only in overdamped adiabatically driven systems [73]. Our ratchet is the first one in which the coherency has been measured in the non-adiabatically driven regime.

7.6 Conclusions

We have experimentally explored the transition from a periodically to a quasiperiodically driven ratchet. The symmetries of the periodic ratchet were generalized to account for driving with incommensurate frequencies. We studied two cases, namely additive and multiplicative driving. In the case of additive driving we found that in the quasiperiodic limit the symmetries of the periodic ratchet are restored. This was shown by measuring the phase shift as a function of pq, our measure of quasiperiodicity. In the case of multiplicative driving the ratchet current is suppressed completely in the quasiperiodic limit, in accordance with symmetry considerations.

The resonances in the spectrum of the multiplicatively driven ratchet are broadened by finite-time driving, as discussed in section 7.4.4. Therefore incommensurate driving frequencies can still yield a nonzero ratchet current in practice, if they are close to frequencies with small p/q. This

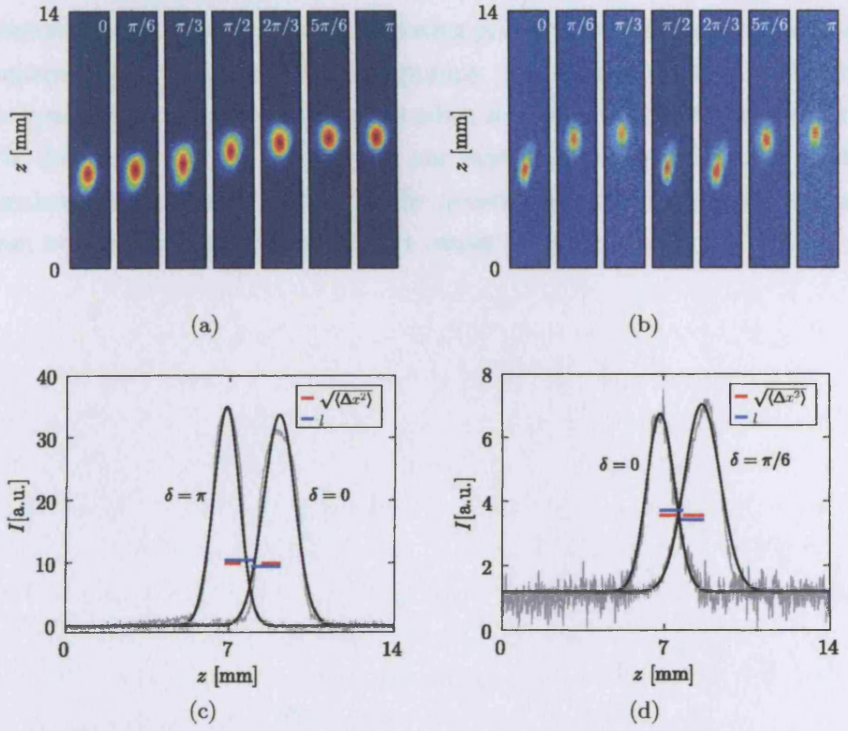

Figure 7.8: Coherency of the multiplicatively driven quasiperiodic ratchet. (*a*) Fluorescence images of the atom cloud after 26 ms of driving with $\omega_1 = \omega_2 = 100$ kHz ($p/q = 1/1$). (*b*) Fluorescence images of the atom cloud after 156 ms of driving with $\omega_1 = 100$ kHz and $\omega_2 = 33\frac{1}{3}$ kHz ($p/q = 1/3$). Each image is labelled by the driving phase δ. (*c*) Intensity profiles of the fluorescence images of the atom cloud for $p/q = 1/1$, and (*d*) for $p/q = 1/3$. The mean spread $\langle \Delta x \rangle$ and displacement l due to the driving are indicated. The black lines are fits of a Gaussian to the data, the Gaussian width is equal to $\langle \Delta x \rangle$. The Peclet numbers are $Pe = 4.3 \pm 0.5$ and $Pe = 2.8 \pm 0.6$ for $p/q = 1/1$ and $p/q = 1/3$ respectively, indicating the ratchet acts coherently.

has to be kept in mind when designing a multifrequency driving to control a ratchet. The results in this chapter show that it is possible however to precisely control the ratchet current by just changing a single driving frequency.

We also showed that our ratchet acts coherently, something that is essential when one thinks about creating practical devices such as particle separators or nano-scale electron pumps. An interesting open question is how the ratchet current changes when a potential gradient is present. As the ratchet works robustly in our experiment it is clear that work against a gradient can be done, the question is how steep the gradient can become before uphill transport ceases completely.

Chapter 8

Conclusion

Over the last decade impressive progress has been made in both experimental implementations and theoretical understanding of ratchets. Systems ranging from Josephson junction arrays to optically trapped beads and artificial molecular devices have been used to experimentally show several aspects of ratchets. Theoretical understanding has come mainly in the form of symmetry analysis. We have been in a position to make a contribution to these developments. In the following, we will give a brief overview of what we have accomplished so far, what interesting open questions are left and where to go from here.

We create cold atom ratchets by phase modulating one of the beams of an optical lattice. When all symmetries of the system are broken, this induces directed transport of the atoms through the lattice. This directed transport is caused by rectification of either the driving force or fluctuations. We demonstrated under which conditions these types of rectification occur. Rectification of the driving force is a deterministic process, the amplitude of which scales approximately inversely with the third power of the driving frequency. Rectification of fluctuations is a resonant process, it is strongest when the driving frequency matches the vibrational frequency of the atoms in the wells of the optical lattice. We demonstrate rectification of fluctuations by showing the velocity of directed transport as a function of the photon scattering rate exhibits stochastic resonance. The atoms act as Brownian motors when fluctuations are rectified, and we have been able to show that resonant activation is the underlying mechanism of operation of these Brownian motors.

Current reversals are an important characteristic of ratchets, and they have technological importance for particle separation purposes. We have shown single and double current reversals as a function of driving frequency, driving amplitude and scattering rate. These reversals, as well as other characteristics such as resonant activation and stochastic resonance, qualitatively match the picture of a ratchet we obtain from numerical simulations.

The ratchet transport is controlled by symmetries of the system. We generally break the temporal symmetry of the system by a time-asymmetric driving force. We also show that for a system with symmetric driving and a symmetric potential, directed transport can be caused by dissipation-induced breaking of time-reversal symmetry. This happens in the limit of small driving amplitude and large dissipation. We found that the current has a sinusoidal dependence on the phase difference between the different harmonics of our bi-harmonic driving. Dissipation introduces a phase shift in this dependence, and we used this phase shift to characterize time-reversal symmetry breaking.

We also studied quasiperiodic driving of a cold atom ratchet, and examined the relationship between symmetries and transport in this case. We employed two different forms of quasiperiodic driving, additive and multiplicative. In the additive case we measured again the phase shift of the current, and used this to show that in the limit of quasiperiodic driving the phase shift is equal to that of the bi-harmonic driving. Therefore in this limit the symmetries of bi-harmonic driving control the ratchet transport. In the multiplicative case we measured the amplitude of the sinusoid we obtained from scanning the phase of one of the driving harmonics. This amplitude drops to zero in the limit of quasiperiodic driving, showing that a quasiperiodic symmetry, which forbids directed transport, is restored. When scanning one of the driving frequencies around the other one, we found a characteristic peak spectrum with transport occurring only for certain ratios of driving frequencies, again as a consequence of symmetries. We have characterized these peaks spectroscopically, and concluded that their shape is determined by the length of driving. Finally, we investigated the coherency of transport with multiplicative driving and found large coherencies, with Peclet numbers up to 4.3, for certain driving parameters.

Now we would like to say a few words about what we can expect from cold atom ratchets in the future. A large number of new ratchet geometries, with corresponding symmetries, have been put forward recently. These include the vibrational and gating ratchets [107, 118], and ratchets with a dc bias [119]. The vibrational ratchet employs two driving frequencies that can be orders of magnitude different, and provides a way to detect frequencies well above a detector bandwidth by monitoring the interplay between the high and the low frequency signal [107]. The gating ratchet employs a modulation of the potential simultaneously with the application of a driving force. This yields yet another way to explore the symmetries of bi-harmonic as well as quasiperiodic driving. The ratchet with dc bias can potentially answer an important open question about the microscopic dynamics underlying the transport. It is predicted that atoms in most of the phase space will accelerate downhill, and only some islands will show stable transport [119]. This should confirm whether the atoms 'sticking' to the island [76] or the higher level sum rule [79] gives a better description of the dynamics.

An important distinction has to be made between ratchets that are underdamped, overdamped or Hamiltonian. All cold atoms ratchets have so far operated in the underdamped regime, most other types of ratchet systems operate in the overdamped regime. It is however possible to use far-detuned optical lattices to create a purely Hamiltonian ratchet. This would also open up the possibility of using BECs or very cold thermal atom clouds to obtain a tunneling rectification mechanism. Even ratchets with collective effects, where the ratchet current depends on the interaction strength between the atoms, can be imagined. We have built a new setup that employs a Ti:Sapphire laser capable of creating such a Hamiltonian ratchet. A QUIC trap [120] has been incorporated into the setup as well to enable the production of a BEC. We are looking forward to using this setup to explore these new types of ratchets.

One of the most important open questions in our opinion is that of the coherency and efficiency of transport. To be able to make the step from the physics of ratchets to their practical applications, it is crucial to characterize and compare the performance of different types of ratchets. We have made a first step by determining the coherency of our quasiperiodic ratchet, but this was by no means an exhaustive

exploration of the phase space of even that ratchet. Our new setup will be able to address this question better than the one described in this thesis. The most important improvement that has been made in this regard is the inclusion of a camera that can take a fluorescence image every 2.5 ms. This will enable the reliable determination of the effective diffusion coefficient, something that is needed to calculate the ratchet efficiency.

To conclude, we foresee cold atom systems continuing to play a large role in experimentally modelling different types of ratchets. New setups to do just that are being built by several groups, including ours. There is a lot of new physics to explore, and we are looking forward with anticipation to developments in this field.

Appendix A

Caesium data

A.1 General properties

In table A.1 we present the most important properties of ^{133}Cs for laser cooling experiments. A complete overview of all relevant data can be found in [121].

A.2 Spectroscopic data

In table A.2 we present the most important spectroscopic data for the D_2 transition in caesium. A complete overview can again be found in [121].

The saturated absorption spectra and error signals for the $F = 4 \rightarrow F'$ and the $F = 3 \rightarrow F'$ transitions are given in figures A.1 and A.2 respectively. The error signal is the first derivative of the absorption spectrum for each transition. This error signal is used in a feedback loop

Quantity	Symbol	Value
mass (^{133}Cs)	m	$2.21 \cdot 10^{-25}$ kg
atomic number		55
melting point	T_{melt}	28.7° C
recoil velocity	$v_{rec} = \hbar k/m$	3.51 mm/s
recoil energy	$E_{rec} = (\hbar k)^2/2m$	$1.37 \cdot 10^{-30}$ J
recoil frequency	$\nu_{rec} = E_{rec}/h$	2.07 kHz
recoil temperature	$T_{rec} = E_{rec}/k_B$	198 nK

Table A.1: General properties of ^{133}Cs.

Quantity	Symbol	Value
nuclear spin	I	7/2
wavelength (D_2)	λ	852.125 nm
wavenumber (D_2)	$k = 2\pi/\lambda$	$7.37 \cdot 10^6$ m^{-1}
natural linewidth (D_2)	Γ	$2\pi \cdot 5.22$ MHz
saturation intensity (D_2)	I_s	1.12 mW/cm^2
Doppler temperature	$T_D = \hbar\Gamma/2k_B$	125.2 μK
Zeeman shift of $6S_{1/2}$ $F = 4$		351 kHz/G$\times m_F$
Zeeman shift of $6P_{3/2}$ $F' = 5$		560 kHz/G$\times m_{F'}$

Table A.2: Spectroscopic data for the D_2 transition in caesium.

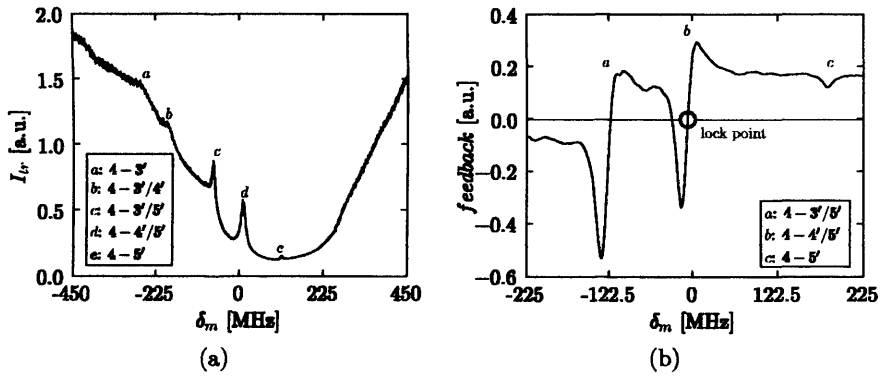

Figure A.1: (a) Saturated absorption spectrum and (b) error signal of the transitions from the $F = 4$ level. The lock point for the master laser on the $4 \rightarrow 4'/5'$ transition is indicated in (b).

to lock the laser frequency to the chosen transition. The feedback is given to the piezo-element that controls the grating for slow variations and to the laser current for fast variations. The lock points of the cooling and repumping lasers are indicated in the figures.

A.3 Level diagram

In figure A.3 we show an energy level diagram for the $6S_{1/2}$, $6P_{1/2}$ and $6P_{3/2}$ states of ^{133}Cs. Laser cooling and repumping are done on the $F = 4 \rightarrow F' = 5$ and $F = 3 \rightarrow F' = 4$ transitions of the D_2 line.

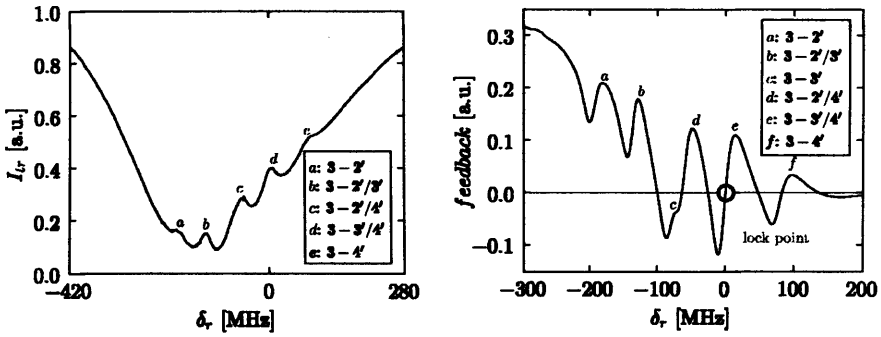

Figure A.2: (*a*) Saturated absorption spectrum and (*b*) error signal of the transitions from the $F = 3$ level. The lock point for the repumper laser on the $3 \rightarrow 3'/4'$ transition is indicated in (*b*).

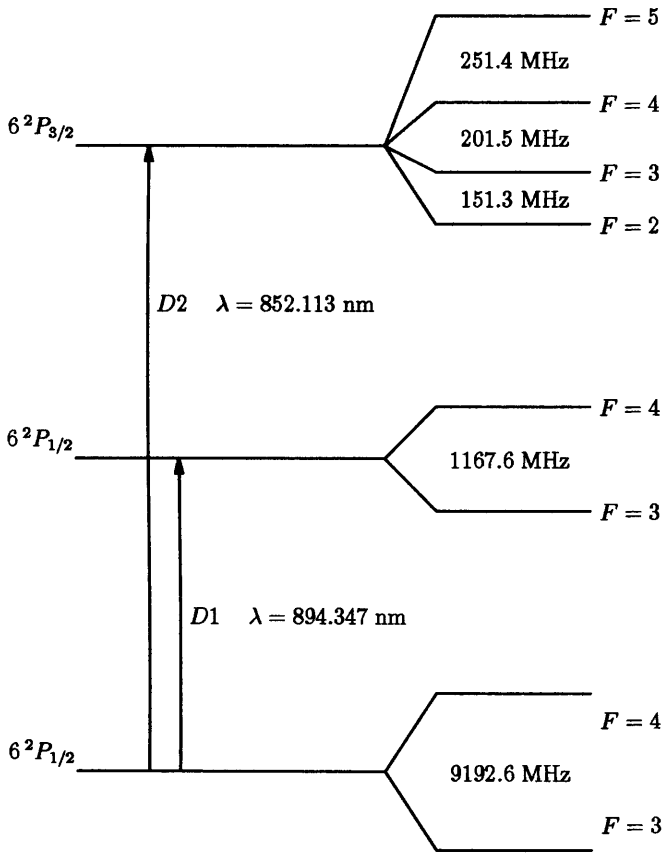

Figure A.3: Energy level diagram of the ground state and lowest two excited states of ^{133}Cs (not to scale).

Appendix B

Pump-probe spectroscopy

In this appendix we will show that the vibrational frequency that is measured with pump-probe spectroscopy, in a configuration as discussed in section 3.2, is the one in the direction of the probe. We will also estimate the error that is introduced by a probe beam that is slightly off-axis.

The electric fields for the umbrella lattice are given by [51]

$$E_{\pm} = \frac{1}{\sqrt{2}} E_0 e^{-ikz}[\mp 1 + \frac{1}{3} e^{i(2k_{\parallel} z - k_{\perp} x)} + \frac{2}{3}\cos[\frac{\sqrt{3}k_{\perp} y}{2}] e^{i(2k_{\parallel} z + k_{\perp} x/2)}]$$
$$E_z = \frac{1}{\sqrt{3}} E_0 \tan(\theta) \sin[\frac{\sqrt{3}k_{\perp} y}{2}] e^{-i(kz + k_{\perp} x/2)}, \tag{B.1}$$

where $k_{\parallel} = k\frac{1+\cos(\theta)}{2}$ and $k_{\perp} = k\sin(\theta)$. The axial beam of the optical lattice is propagating in the -z direction here, and the circular polarizations are given by $\hat{\varepsilon}_{\pm} = \mp\frac{\hat{\varepsilon}_x \pm i\hat{\varepsilon}_y}{\sqrt{2}}$. For a probe beam co-propagating with the axial pump beam and polarized along x, the electric field is

$$\overline{E}_p = \frac{1}{\sqrt{2}}(\hat{\varepsilon}_- - \hat{\varepsilon}_+) E_p e^{-ikz}. \tag{B.2}$$

The matrix element of the Raman operator $\langle n'|(E_p)_q E_q|n\rangle$, where $q = +, -, z$, can now be calculated. The transition amplitude is proportional to the square of the matrix element.

$$E^{\dagger}_{p,\pm} E_{0,\pm} = \mp\frac{1}{2} E^{\dagger}_p E_0 [\mp 1 + \frac{1}{3} e^{i(2k_{\parallel} z - k_{\perp} x)} + \frac{2}{3}\cos[\frac{\sqrt{3}k_{\perp} y}{2}] e^{i(2k_{\parallel} z + k_{\perp} x/2)}]. \tag{B.3}$$

The minima of the optical potential are given by

$$R^{(-)}_{l,m,n} = l\frac{\lambda_\perp}{3}e_x + (2m+l)\frac{\lambda_\perp}{\sqrt{3}}e_y + (3n+l)\frac{\lambda_\parallel}{6}e_z, \tag{B.4}$$

$$R^{(+)}_{l,m,n} = l\frac{\lambda_\perp}{3}e_x + (2m+l)\frac{\lambda_\perp}{\sqrt{3}}e_y + (3n+l+\frac{1}{2})\frac{\lambda_\parallel}{6}e_z \tag{B.5}$$

for the σ^- and the σ^+ polarized sites respectively.

The inner part of the Raman operator matrix element can now be developed to first order around a minimum of the right polarization. Here we take (0,0,0) for the σ^- polarization and $(0,0,\lambda_\parallel/4)$ for the σ^+ polarization. This gives

$$\begin{aligned} E^\dagger_{p,+}E_{0,+} &= -\frac{1}{2}E^\dagger_p E_0[-1+\frac{1}{3}(1+i(2k_\parallel z - k_\perp x)) + \frac{2}{3}(1+i(2k_\parallel z + k_\perp x/2)) \\ &= \frac{1}{2}E^\dagger_p E_0[-i(2k_\parallel(z-\lambda_\parallel/4))] \qquad \text{(B.6)} \\ E^\dagger_{p,-}E_{0,-+} &= \frac{1}{2}E^\dagger_p E_0[1+\frac{1}{3}(1+i(2k_\parallel z - k_\perp x)) + \frac{2}{3}(1+i(2k_\parallel z + k_\perp x/2)) \\ &= \frac{1}{2}E^\dagger_p E_0[-i(2k_\parallel(z-\lambda_\parallel/4))]. \qquad \text{(B.7)} \end{aligned}$$

Now the transition amplitude is equal to $\langle n'|(E_p)_+E_+|n\rangle^2 + \langle n'|(E_p)_-E_-|n\rangle^2$, which shows that only transitions with $\Delta n_z = \pm 1$ will be excited. Therefore applying a probe beam along the z-axis will measure the vibrational frequency along that z-axis. It can easily be shown that changing the polarization of the probe beam so it is polarized along y leads to the same conclusion. In a similar way it can be shown that applying a probe beam along the x- or y-axis will yield transition with $\Delta n_x = \pm 1$ or $\Delta n_y = \pm 1$ respectively (note that there is a very small probability of exciting a transition $\Delta n_z = \pm 1$, equal to $\frac{(k-k_\parallel)^2}{k^2} \simeq 0.005$.

For a probe beam in the yOz-plane making a small angle ϕ with the z-axis, as in our experiment, the ratio of $\Delta n_z = \pm 1$ and $\Delta n_y = \pm 1$ transitions excited is given by

$$\frac{A_z^2}{A_y^2} = \frac{(\cos(\phi) - \frac{1}{2} + \frac{1}{4}\sqrt{3})^2}{\sin(\phi)^2}. \tag{B.8}$$

For an angle $\phi = 7°$ this ratio is $\simeq 50$. We can therefore conclude that our probe beam, which makes this angle with the z-axis, measures the

vibrational frequency in the z-direction with an error of $< 2\%$.

Bibliography

[1] E. L. Raab, M. Prentiss, A. Cable, S. Chu and D. E. Pritchard, *Trapping of neutral sodium atoms with radiation pressure*, Phys. Rev. Lett. **59**, 2631 (1987)

[2] M. H. Anderson, J. R. Ensher, M. R. Matthews, C. E. Wieman and E. A. Cornell, *Observation of Bose-Einstein condensation in a dilute atomic vapor*, Science **269**, 198 (1995)

[3] M. von Smoluchowski, *Experimentell nachweisbare, der üblichen thermodynamik widersprechende molekularphänomene*, Physik. Zeitschr. **13**, 1069 (1912)

[4] H. Leff and A. Rex, editors, *Maxwell's Demon 2*, IoP Publishing Ltd (2003)

[5] L. Brillouin, *Can the rectifier become a thermo-dynamical demon?*, Phys. Rev. **78**, 627 (1950)

[6] P. Landa, *Noise-induced transport of Brownian particles with consideration for their mass*, Phys. Rev. E **58**, 1325 (1998)

[7] T. Tsong and R. Astumian, *Absorption and conversion of electric field energy by membrane bound ATPase*, Bioelectrochem. Bioenerg. **15**, 457 (1986)

[8] A. Ajdari and J. Prost, *Mouvement induit par un potentiel periodique de basse symmetrie: dielectrophorèse pulsée*, C. R. Acad. Sci. Paris **315**, 1635 (1992)

[9] M. Magnasco, *Forced thermal ratchets*, Phys. Rev. Lett. **71**, 1477 (1993)

[10] M. Magnasco, *Molecular combustion motors*, Phys. Rev. Lett. **72**, 2656 (1994)

[11] J. Prost, J.-F.Chawin, L. Peliti and A. Ajdari, *Asymmetric pumping of particles*, Phys. Rev. Lett. **72**, 2652 (1994)

[12] R. Astumian and M. Bier, *Fluctuation-driven ratchets: Molecular motors*, Phys. Rev. Lett. **72**, 1766 (1994)

[13] C. R. Doering., W. Horsthemke and J. Riordan, *Nonequilibrium fluctuation-induced transport*, Phys. Rev. Lett. **72**, 2987 (1994)

[14] J.-F. Chauwin, A. Ajdari and J. Prost, *Force-free motion in asymmetric structures: a mechanism without diffusive steps*, Eur. Phys. Lett. **27**, 421 (1994)

[15] R. Bartussek, P. Hänggi and J. Kissner, *Periodically rocked thermal ratchets*, Eur. Phys. Lett. **28**, 459 (1994)

[16] J. Rousselet, L. Salome, A. Ajdari and J. Prost, *Directional motion of Brownian particles induced by a periodic asymmetric potential*, Nature **370**, 446 (1994)

[17] L. Faucheux, L. Bourdieu, P. Kaplan and A. Libchaber, *Optical thermal ratchet*, Phys. Rev. Lett. **74**, 1504 (1994)

[18] A. van Oudenaarden and S. Boxer, *Brownian ratchets: Molecular separations in lipid bilayers supported on patterned arrays*, Science **285**, 1049 (1999)

[19] H. Linke, T. Humphrey, A. Löfgren, A. Sushkov, R. Newbury and P. Omling, *Experimental tunneling ratchets*, Science **286**, 2314 (1999)

[20] A.-L. Barabasi, B. Janko, C. Lee and I. Derenyi, *Reducing vortex densities and transporting vortices in superconductors*, U.S. Patent 6469880 (2002)

[21] V. Serreli, C.-F. Lee, E. Kay and D. Leigh, *A molecular information ratchet*, Nature **445**, 523 (2007)

[22] P. Reimann, M. Grifoni and P. Hänggi, *Quantum ratchets*, Phys. Rev. Lett. **79**, 10 (1997)

[23] C. Jarzynski, *Nonequilibrium equality for free energy differences*, Phys. Rev. Lett. **78**, 2690 (1997)

[24] T. W. Hänsch and A. L. Schawlow, *Cooling of gases by laser radiation*, Opt. Commun. **13**, 68 (1975)

[25] S. Chu, L. Hollberg, J. E. Bjorkholm, A. Cable and A. Ashkin, *Three-dimensional viscous confinement and cooling of atoms by resonance radiation pressure*, Phys. Rev. Lett. **55**, 48 (1985)

[26] B. DeMarco and D. S. Jin, *Onset of Fermi degeneracy in a trapped atomic gas*, Science **285**, 1703 (1999)

[27] H. Metcalf and P. van der Straten, *Laser Cooling and Trapping*, Springer-Verlag, New York (1999)

[28] M. Greiner, O. Mandel, T. Esslinger, T. W. Hänsch and I. Bloch, *Quantum phase transition from a superfluid to a Mott insulator in a gas of ultracold atoms*, Nature **415**, 39 (2002)

[29] C. Regal, M. Greiner and D. Jin, *Observation of resonance condensation of fermionic atom pairs*, Phys. Rev. Lett. **92**, 040403 (2004)

[30] M. Zwierlein, C. Stan, C. Schunck, S. Raupach, A. Kerman and W. Ketterle, *Condensation of pairs of fermionic atoms near a Feshbach resonance*, Phys. Rev. Lett. **92**, 120403 (2004)

[31] F. Moore, J. Robinson, C. Bharucha, B. Sundaram and M. Raizen, *Atom optics realization of the quantum δ-kicked rotor*, Phys. Rev. Lett. **75**, 4598 (1995)

[32] C. Mennerat-Robilliard, D. Lucas, S. Guibal, J. Tabosa, C. Jurczak, J.-Y. Courtois and G. Grynberg, *Ratchet for cold rubidium atoms: The asymmetric optical lattice*, Phys. Rev. Lett. **82**, 000851 (1999)

[33] R. Gommers, P. Douglas, S. Bergamini, M. Goonasekera, P. H. Jones and F. Renzoni, *Resonant activation in a nonadiabatically driven optical lattice*, Phys. Rev. Lett. **94**, 143001 (2005)

[34] R. Gommers, S. Bergamini and F. Renzoni, *Dissipation-induced symmetry breaking in a driven optical lattice*, Phys. Rev. Lett. **95**, 073003 (2005)

[35] R. Gommers, S. Denisov and F. Renzoni, *Quasiperiodically driven ratchets for cold atoms*, Phys. Rev. Lett. **96**, 240604 (2006)

[36] R. Gommers, M. Brown and F. Renzoni, *Symmetry and transport in a cold atom ratchet with multifrequency driving*, Phys. Rev. A **75**, 053406 (2007)

[37] M. Levenson and S. Kano, *Introduction to Nonlinear Spectroscopy*, Academic Press, Boston (1988)

[38] L. Ricci, M. Weidemüller, T. Esslinger, A. Hemmerich, C. Zimmermann, V. Vuletic, W. König and T. Hänsch, *A compact grating-stabilized diode laser system for atomic physics*, Opt. Comm. **117**, 541 (1995)

[39] R. Lang, *Injection locking properties of a semiconductor laser*, IEEE J. Quantum Electronics **18**, 876 (1982)

[40] O. Schmidt, K.-M. Knaak, R. Wynands and D. Meschede, *Cesium saturation spectroscopy revisited: How to reverse peaks and observe narrow resonances*, Appl. Phys. B **59**, 167 (1994)

[41] C. Cohen-Tannoudji, *Atomic motion in laser light*, Fundamental Systems in Quantum Optics (Les Houches 1990, Session LIII), Elsevier, Amsterdam (1992)

[42] P. D. Lett, R. N. Watts, C. I. Westbrook, W. D. Phillips, P. L. Gould and H. J. Metcalf, *Observation of atoms laser cooled below the Doppler limit*, Phys. Rev. Lett. **61**, 169 (1988)

[43] J. Dalibard and C. Cohen-Tannoudji, *Laser cooling below the Doppler limit by polarization gradients: simple theoretical-models*, J. Opt. Soc. Am. B **6**, 2023 (1989)

[44] P. Ungar, D. Weiss, E. Riis and S. Chu, *Optical molasses and multilevelatoms: theory*, J. Opt. Soc. Am. B **6**, 2058 (1989)

[45] C. Westbrook, R. Watts, C. Tanner, S. Rolston, W. Phillips and P. Lett, *Localization of atoms in a three-dimensional standing wave*, Phys. Rev. Lett. **65**, 33 (1990)

[46] R. Dicke, *The effect of collisions upon the Doppler width of spectral lines*, Phys. Rev. **89**, 472 (1953)

[47] G. Grynberg, B. Lounis, P. Verkerk, J.-Y. Courtois and C. Salomon, *Quantized motion of cold cesium atoms in two- and three-dimensional optical potentials*, Phys. Rev. Lett. **70**, 2249 (1993)

[48] P. Verkerk, B. Lounis, C. Salomon, C. Cohen-Tannoudji, J.-Y. Courtois and G. Grynberg, *Dynamics and spatial order of cold cesium atoms in a periodic optical potential*, Phys. Rev. Lett. **68**, 3861 (1992)

[49] P. S. Jessen, C. Gerz, P. D. Lett, W. D. Phillips, S. L. Rolston, R. J. C. Spreeuw and C. I. Westbrook, *Observation of quantized motion of Rb atoms in an optical field*, Phys. Rev. Lett. **69**, 49 (1992)

[50] A. Hemmerich and T. Hänsch, *Two-dimensional atomic crystal bound by light*, Phys. Rev. Lett. **70**, 410 (1993)

[51] K. I. Petsas, A. B. Coates and G. Grynberg, *Crystallography of optical lattices*, Phys. Rev. A **50**, 5173 (1994)

[52] C. Mennerat-Robilliard, L. Guidoni, K. Petsas, P. Verkerk, J.-Y. Courtois and G. Grynberg, *Bright optical lattices in a longitudinal magnetic field: Experimental study of the oscillating and jumping regimes*, Eur. Phys. J. D **1**, 33 (1998)

[53] F. R. Carminati, M. Schiavoni, Y. Todorov, F. Renzoni and G. Grynberg, *Pump-probe spectroscopy of atoms cooled in a 3D lin⊥lin optical lattice*, Eur. Phys. J. D **22**, 311 (2003)

[54] J. Y. Courtois and G. Grynberg, *Probe transmission in one-dimensional optical molasses: Theory for linearly cross-polarized cooling beams*, Phys. Rev. A **46**, 7060 (1992)

[55] F.-R. Carminati, L. Sanchez-Palencia, M. Schiavoni, F. Renzoni and G. Grynberg, *Rayleigh scattering and atomic dynamics in dissipative optical lattices*, Phys. Rev. Lett. **90**, 043901 (2003)

[56] L. Sanchez-Palencia, P. Horak and G. Grynberg, *Spatial diffusion in a periodic optical lattice: revisiting the Sisyphus effect*, Eur. Phys. J. D **18**, 353 (2002)

[57] G. Raithel, G. Birkl, A. Kastberg, W. Phillips and S. Rolston, *Cooling and localization dynamics in optical lattices*, Phys. Rev. Lett. **78**, 630 (1997)

[58] P. Reimann, *Brownian motors: noisy transport far from equilibrium*, Phys. Rep. **361**, 57 (2002)

[59] J. Parrondo, *Efficiency of Brownian motors*, eEC HC&M Network on Complexity and Chaos (#ERBCHRX-CT940546), ISI Foundation, Italy (1996), unpublished

[60] G. Harmer and D. Abbott, *Parrondo's paradox*, Statist. Sci. **14**, 206 (1999)

[61] L. Gorre, E. Ioannidis and P. Silberzan, *Rectified motion of a mercury drop in an asymmetric structure*, Eur. Phys. Lett. **33**, 267 (1996)

[62] C. de Souza Silva, J. V. de Vondel, M. Morelle and V. Moshchalkov, *Controlled multiple reversals of a ratchet effect*, Nature **440**, 651 (2006)

[63] S. Denisov, S. Flach, A. A. Ovchinnikov, O. Yevtushenko and Y. Zolotaryuk, *Broken space-time symmetries and mechanisms of rectification of ac fields by nonlinear (non)adiabatic response*, Phys. Rev. E **66**, 041104 (2002)

[64] Y. Castin and J. Dalibard, *Quantization of atomic motion in optical molasses*, Eur. Phys. Lett. **14**, 761 (1991)

[65] P. Jung, J. Kissner and P. Hänggi, *Regular and chaotic transport in asymmetric periodic potentials: Inertia ratchets*, Phys. Rev. Lett. **76**, 3436 (1996)

[66] D. Dan, M. Mahato and A. Jayannavar, *Multiple current reversals in forced inhomogeneous ratchets*, Phys. Rev. E **63**, 056307 (2001)

[67] J. Parrondo, *Reversible ratchets as Brownian particles in an adiabatically changing periodic potential*, Phys. Rev. Lett. **57**, 7297 (1998)

[68] H. Linke, M. Downton and M. Zuckermann, *Performance characteristics of Brownian motors*, Chaos **15**, 026111 (2005)

[69] H. Zhou and Y. Chen, *Chemically driven motility of Brownian particles*, Phys. Rev. Lett. **77**, 194 (1996)

[70] I. Derényi, M. Bier and R. Astumian, *Generalized efficiency and its application to microscopic engines*, Phys. Rev. Lett. **83**, 903 (1999)

[71] H. Wang and G. Oster, *The Stokes efficiency for molecular motors and its applications*, Eur. Phys. Lett. **57**, 134 (2002)

[72] D. Suzuki and T. Munakata, *Rectification efficiency of a Brownian motor*, Phys. Rev. E **68**, 021906 (2003)

[73] S. Roy, D. Dan and A. Jayannavar, *Giant coherence in driven systems*, J. Stat. Mech. **09**, P09012 (2006)

[74] M. Schnitzer and S. Block, *Kinesin hydrolyses one ATP per 8-nm step*, Nature **388**, 386 (1997)

[75] K. Visscher, M. Schnitzer and S. Block, *Single kinesin molecules studied with a molecular force clamp*, Nature **400**, 184 (1999)

[76] S. Denisov and S. Flach, *Dynamical mechanism of dc current generation in driven Hamiltonian systems*, Phys. Rev. E **64**, 056236 (2001)

[77] P. Douglas, S. Bergamini and F. Renzoni, *Tunable Tsallis distributions in dissipative optical lattices*, Phys. Rev. Lett. **96**, 110601 (2006)

[78] S. Denisov, J. Klafter and M. Urbakh, *Manipulation of dynamical systems by symmetry breaking*, Phys. Rev. E **66**, 046203 (2002)

[79] H. Schanz, T. Dittrich and R. Ketzmerick, *Directed chaotic transport in Hamiltonian ratchets*, Phys. Rev. E **71**, 026228 (2005)

[80] S. Denisov, *Underdamped ratchets* (2006), private communication

[81] H. A. Kramers, *Brownian motion in a field of force and the diffusion model of chemical reactions*, Physica **7**, 284 (1940)

[82] M. Dykman, H. Rabitz, V. Smelyanskiy and B. Vugmeister, *Resonant directed diffusion in nonadiabatically driven systems*, Phys. Rev. Lett. **79**, 1178 (1997)

[83] V. N. Smelyanskiy, M. I. Dykman, H. Rabitz and B. E. Vugmeister, *Fluctuations, escape, and nucleation in driven systems: Logarithmic susceptibility*, Phys. Rev. Lett. **79**, 3113 (1997)

[84] M. Dykman, B. Golding, L. McCann, V. Smelyanskiy, D. Luchinsky, R. Mannella and P. McClintock, *Activated escape of periodically driven systems*, Chaos **11**, 587 (2001)

[85] A. Lorke, S. Wimmer, B. Jager, J. Kotthaus, W. Wegschneider and M. Bichler, *Far-infrared and transport properties of antidot arrays with broken symmetry*, Physica B **251**, 312 (1998)

[86] M. Switkes, C. Marcus, K. Campman and A. Gossard, *An adiabatic quantum electron pump*, Science **283**, 1905 (1999)

[87] S. Weiss, D. Koelle, J. Müller, R. Gross and K. Barthel, *Ratchet effect in dc SQUIDs*, Eur. Phys. Lett. **51**, 499 (2000)

[88] J. Villegas, S. Savel'ev, F. Nori, E. Gonzales, J. Anguita, R. Garcia and J. Vicent, *A superconducting reversible rectifier that controls the motion of magnetic flux quanta*, Science **302**, 1188 (2003)

[89] D. van der Meer, P. Reimann, K. van der Weele and D. Lohse, *Spontaneous ratchet effect in a granular gas*, Phys. Rev. Lett. **92**, 184301 (2004)

[90] D. Shalóm and H. Pastoriza, *Vortex motion rectification in Josephson junction arrays with a ratchet potential*, Phys. Rev. Lett. **94**, 177001 (2005)

[91] H. Linke, B. Alemán, L. Melling, M. Taormina, M. Francis, C. Dow-Hygelund, V. Narayanan, R. Taylor and A. Stout, *Self-propelled Leidenfrost droplets*, Phys. Rev. Lett. **96**, 154502 (2006)

[92] A. Rahman, M. Sanyal, R. Gangopadhayy, A. De and I. Das, *Evidence of a ratchet effect in nanowires of a conducting polymer*, Phys. Rev. B **73**, 125313 (2006)

[93] C. Mennerat-Robilliard, D. Lucas and G. Grynberg, *Modelling a ratchet with cold atoms in an optical lattice*, Appl. Phys. A **75**, 213 (2001)

[94] P. H. Jones, M. Goonasekera and F. Renzoni, *Rectifying fluctuations in an optical lattice*, Phys. Rev. Lett. **93**, 073904 (2004)

[95] A. Ajdari, J. Lewiner, J. Prost and J. Viovy, *Pompage sélectif*, French Patent 9311346 (1993)

[96] M. Devoret, J. Martinis, D. Esteve and J. Clarke, *Resonant activation from the zero-voltage state of a current-biased Josephson junction*, Phys. Rev. Lett. **53**, 1260 (1984)

[97] C. R. Doering. and J. C. Gadoua, *Resonant activation over a fluctuating barrier*, Phys. Rev. Lett. **69**, 2318 (1992)

[98] R. Mantegna and B. Spagnolo, *Experimental investigation of resonant activation*, Phys. Rev. Lett. **84**, 3025 (2000)

[99] C. Schmitt, B. Dybiec, P. Hänggi and C. Bechinger, *Stochastic resonance vs. resonant activation*, Eur. Phys. Lett. **74**, 937 (2006)

[100] B. McNamara, K. Wiesenfeld and R. Roy, *Observation of stochastic resonance in a ring laser*, Phys. Rev. Lett. **60**, 2626 (1988)

[101] J. Douglass, L. Wilkens, E. Pantazelou and F. Moss, *Noise enhancement of information transfer in crayfish mechanoreceptors by stochastic resonance*, Nature **365**, 337 (1993)

[102] R. Benzi, A. Sutera and A. Vulpiani, *The mechanism of stochastic resonance*, J. Phys. A **14**, L453 (1981)

[103] S. Fauve and F. Heslot, *Stochastic resonance in a bistable system*, Phys. Lett. A **97**, 5 (1983)

[104] W. Schneider and K. Seeger, *Harmonic mixing of microwaves by warm electrons in germanium*, Appl. Phys. Lett. **8**, 133 (1966)

[105] F. Marchesoni, *Harmonic mixing signal: Doubly dithered ring laser gyroscope*, Phys. Lett. A **119**, 221 (1986)

[106] S. Flach, O. Yevtushenko and Y. Zolotaryuk, *Directed current due to broken time-space symmetry*, Phys. Rev. Lett. **84**, 2358 (2000)

[107] M. Borromeo and F. Marchesoni, *Vibrational ratchets*, cond-mat 0601609 (2006)

[108] P. Horowitz and W. Hill, *The Art of Electronics*, Cambridge University Press (1980)

[109] M. Brown, *Low-frequency behavior of underdamped ratchets* (2007), private communication

[110] M. Schiavoni, L. Sanchez-Palencia, F. Renzoni and G. Grynberg, *Phase control of directed diffusion in a symmetric optical lattice*, Phys. Rev. Lett. **90**, 094101 (2003)

[111] O. Yevtushenko, S. Flach, Y. Zolotaryuk and A. Ovchinnikov, *Rectification of current in ac-driven nonlinear systems and symmetry properties of the Boltzmann equation*, Eur. Phys. Lett. **54**, 141 (2001)

[112] R. Penrose, *The Road to Reality*, Knopf, New York (2005)

[113] G. Crooks, *Entropy production fluctuation theorem and the nonequilibrium work relation for free energy differences*, Phys. Rev. E **60**, 2721 (1999)

[114] D. Evans, E. Cohen and G. Morriss, *Probability of Second Law violations in shearing steady states*, Phys. Rev. Lett. **71**, 2401 (1993)

[115] C. Bustamante, J. Liphardt and F. Ritort, *The nonequilibrium thermodynamics of small systems*, Physics Today **58**, 43 (2005)

[116] P. Sjölund, S. Petra, C. Dion, S. Jonsell, M. Nylén, L. Sanchez-Palencia and A. Kastberg, *Demonstration of a controllable three-dimensional Brownian motor in symmetric potentials*, Phys. Rev. Lett. **96**, 190602 (2006)

[117] E. Neumann and A. Pikovsky, *Quasiperiodically driven Josephson junctions: strange nonchaotic attractors, symmetries and transport*, Eur. Phys. J. B **26**, 219 (2002)

[118] M. Borromeo and F. Marchesoni, *Noise-assisted transport on symmetric periodic substrates*, Chaos 026110 (2005)

[119] S. Denisov, S. Flach and P. Hänggi, *Stationary Hamiltonian transport with dc bias*, Eur. Phys. Lett. **74**, 588 (2006)

[120] T. Esslinger, I. Bloch and T. W. Hänsch, *Bose-Einstein condensation in a quadrupole-Ioffe-configuration trap*, Phys. Rev. A **58**, R2664 (1998)

[121] D. Steck, *Cesium D line data* (2003), `www.steck.us/alkalidata`

Index